Accepted Manuscript

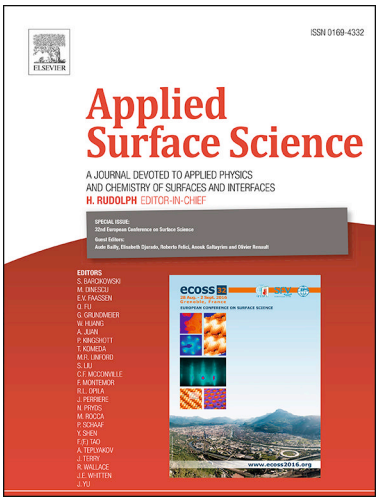

Full Length Article

The evaluation of the photocatalytic activity of magnetic and non-magnetic polymorphs of Fe_2O_3 in natural sunlight exposure: A comparison of photocatalytic activity

M. Aslam, M. Tariq Qamar, Ateeq Ur Rehman, M. Tahir Soomro, Shahid Ali, I.M.I. Ismail, A. Hameed

PII: S0169-4332(18)31192-9
DOI: https://doi.org/10.1016/j.apsusc.2018.04.219
Reference: APSUSC 39218

To appear in: *Applied Surface Science*

Received Date: 20 October 2017
Revised Date: 3 April 2018
Accepted Date: 24 April 2018

Please cite this article as: M. Aslam, M. Tariq Qamar, A. Ur Rehman, M. Tahir Soomro, S. Ali, I.M.I. Ismail, A. Hameed, The evaluation of the photocatalytic activity of magnetic and non-magnetic polymorphs of Fe_2O_3 in natural sunlight exposure: A comparison of photocatalytic activity, *Applied Surface Science* (2018), doi: https://doi.org/10.1016/j.apsusc.2018.04.219

The evaluation of the photocatalytic activity of magnetic and non-magnetic polymorphs of Fe_2O_3 in natural sunlight exposure: a comparison of photocatalytic activity

M. Aslam[1], M. Tariq Qamar[2], Ateeq Ur Rehman[3], M. Tahir Soomro[1], Shahid Ali[4], I.M.I. Ismail[1,5], and A. Hameed[1,6]

[1]Center of Excellence in Environmental Studies, King Abdulaziz University, Jeddah 21589, Saudi Arabia

[2]Department of Chemistry, Forman Christian College (A Chartered University), Ferozepur Road, Lahore, 54600, Pakistan

[3]School of Chemical Engineering, The University of Queensland, St Lucia 4072, Queensland, Australia.

[4]Center of Excellence in Nanotechnology, King Fahd University of Petroleum and Minerals, Dhahran 31261, Saudi Arabia.

[5]Chemistry Department, Faculty of Science, King Abdulaziz University, Jeddah 21589, Saudi Arabia.

[6]National Center for Physics, Quaid-e-Azam University, Islamabad 44000, Pakistan.

[*]Corresponding Author:

Abdul Hameed, PhD

Associate Professor

Centre of Excellence in Environmental Studies (CEES)

King Abdulaziz University, Jeddah

Fax: 00966-12-6952674

ahfmuhammad@gmail.com, afmuhammad@kau.edu.sa

Abstract:

The non-magnetic and magnetic polymorphs of iron oxide (Fe_2O_3) namely: α-Fe_2O_3 (hematite) and γ-Fe_2O_3 (maghemite) respectively, were synthesized by a facile surfactant aided hydrogel route. The synthesized polymorphs were characterized by diffuse reflectance, photoluminescence and raman spectroscopy for optical properties whereas the morphological, structural, chemical and electronic state evaluation were performed by FESEM, HRTEM, XRD, and XPS. The charge transport and the stability of the materials were examined electrochemically. The photocatalytic activity of the synthesized polymorphs was evaluated for the degradation of 2-chlorophenol and 2-nitrophenol in the exposure of the visible region and complete spectrum natural sunlight. Both the polymorphs exhibited a significantly high activity for the degradation of the phenolic substrate in the exposure of the complete spectrum of sunlight, however, the activity in the visible region of the sunlight was relatively lower. A substantial increase in the activity in the visible region was noticed when the polymorphs were exposed to complete spectrum sunlight prior to the photocatalytic experiments. The comparison of the exposed and unexposed samples revealed the induction of defects that served as traps for the excited electrons and increased activity of the polymorphs.

Keywords: α-Fe_2O_3, γ-Fe_2O_3, Natural Sunlight, 2-Chlorophenol, 2-Nitrophenol.

1. Introduction

Heterogeneous photocatalysis is a rapidly emerging technique for efficient and optimum removal of hazardous organic pollutants from the aquatic environment. Despite its utmost importance and numerous impressive material properties with respect to photocatalysis, TiO_2, the most extensively studied photocatalyst with commercial applications, suffers the drawback of insignificant absorption in the visible region, the fast recombination rate of photo-induced electron-hole pairs, less adsorptive sites for target pollutants [1-6]. When used in powder form in the nanoscale, its retrieval from the medium is another issue of concern and limits its wide application. In the last two decades, as a consequence of immense efforts by the scientific community on the modification of TiO_2 for enhancing its activity in the visible region of the spectrum, the exploration and detailed investigation of the active photocatalysts, capable of utilizing a wide spectral range, has been neglected [7-10]. Additionally, the majority of the studies on the subject of photocatalytic decontamination of water, available in the literature, are based on the use of artificial light sources as excitation sources that not only adds to the cost but also limits the utility of the process to academics only. It is now well-established fact that photocatalysis can attain its optimum practical and commercial applicability only with the use of natural sunlight as the excitation source. Additionally, inexpensive and ever-renewable sunlight can engender the cost-effective solution of the environmental issues [11]. As 46% of the solar spectrum falls in the visible region, the use of natural sunlight as an initiator in the photocatalysis demands the in-depth estimation of the photocatalytic activity of the sunlight responsive active photocatalysts [12-14].

Among the existing metal oxide semiconductors, iron (III) oxide (Fe_2O_3), owing to its chemical stability, natural abundance and absorption in the visible region can be an appropriate competitor for photocatalytic environmental applications. The α and γ phases of Fe_2O_3 namely hematite and maghemite respectively have gained considerable attention in photocatalysis [15-20]. Both hematite (α-Fe_2O_3) and maghemite (γ-Fe_2O_3) are n-type semiconductors with the bandgap energy range from 1.9 to 2.2 eV, can utilize ~40% of solar light [21-27]. Among the two polymorphs, α-Fe_2O_3 is antiferromagnetic whereas γ-Fe_2O_3 is ferromagnetic in nature [28, 29], therefore, the issue of the retrieval can be successfully addressed with the use of Fe_2O_3. Recently, based on the development of pure, composite and core-shell magnetic nanoparticles, the reported studies on the retrieval of the photocatalyst from the reaction medium have achieved considerable attention for environmental remediation [30-38]. A score of studies are available in the literature where α-Fe_2O_3 has been used in combination with other photocatalysts such as TiO_2 [39-41], ZnO [42, 43], SiO_2 [44] etc., for enhancing the photocatalytic activity in the visible region of the spectrum. Although γ-Fe_2O_3 has been used by a number of researchers as magnetic support in an effort to make the existing photocatalysts magnetically retrievable [45-49], however, not investigated in detail for its own photocatalytic activity in sunlight exposure. Additionally, the studies evaluating the photocatalytic activity of both the pure polymorphs especially in the natural sunlight exposure are rare.

In the current study, the two polymorphs i.e. α-Fe_2O_3 and γ-Fe_2O_3 were synthesized by adopting a user-friendly identical procedure. The pure powders were characterized optically, electrochemically, structurally and chemically for the spectral

response stability and crystal structure determination. A detailed comparison of the photocatalytic activities of α-Fe_2O_3 and γ-Fe_2O_3 nanoparticles in natural sunlight exposure (complete spectrum of sunlight and visible region of sunlight) was carried out for the degradation as well as mineralization of 2-nitrophenol (2-NP) and 2-chlorophenol (2-CP). Both the polymorphs were re-evaluated after exposure to sunlight for the possible changes in the material under illumination and the effect of these changes on the photocatalytic activity was also estimated. The progress of the degradation and intermediates formed during the reaction were investigated by HPLC whereas TOC was used to monitor mineralization process. The released ions were measured quantitatively by IC. The complete recovery of the polymorphs from the catalyst/substrate suspension was made with the help of an external magnet. Finally, all information obtained by TOC, IC, HPLC, and GCMS are associated to propose the mechanism of degradation. The recovery of both the polymorphs from the catalyst/substrate suspension was estimated by the permanent magnet.

2. Experimental details

The non-magnetic polymorph i.e. α-Fe_2O_3 was synthesized by hydrolyzing the solution of Fe^{3+} ions with KOH. $Fe(NO_3)_3.9H_2O$ (Sigma-Aldrich) was used as the precursor for Fe^{3+} ions. The morphology of α-Fe_2O_3 particles was controlled by the addition of the Triton X-100 as a surfactant. In a typical synthesis, the appropriate amount of Fe^{3+} ions were stirred with Triton X-100 (0.5%) with respect to the weight of Fe^{3+} ions) for 30 minutes at 100 $^{\circ}$C. The surfactant added solution was hydrolyzed by the drop-wise addition of 0.1M KOH. The pH of the solution was adjusted at 9. The suspension was heated at an elevated temperature of 150 $^{\circ}$C for 3 h and aged

overnight. The precipitates were filtered and washed several times with DI water for the complete removal of excessive KOH. The surfactant was removed by repeated washings with 50:50 ethanol-acetone mixture. The washed precipitates were dried for overnight in the vacuum oven at 100 $^{\circ}$C and calcined for 5 h at 400 $^{\circ}$C in the muffle furnace at the heating and cooling rate of 10 $^{\circ}$C /min that resulted in reddish powder. For the synthesis of γ-Fe_2O_3, Fe(II)SO_4 (Sigma-Aldrich) was used as a precursor. The synthetic route was similar to that adopted for α-Fe_2O_3 however, after the calcination at 400 $^{\circ}$C for 5 h in the muffle furnace at the heating and cooling rate of 10 $^{\circ}$C /min that resulted in brown powder. The magnetism of the powder was evaluated by a permanent magnet.

A Perkin Elmer UV-visible diffuse reflectance spectrophotometer (Lambda 650) was used to acquire the solid-state absorption and diffuse reflectance spectra (DRS) of the as-synthesized samples in 190-900 nm range. The acquired %R data, after applying the Kubelka-Munk transformation, was used for the evaluation of the bandgaps. Similarly, the photoluminescence (PL) and Raman shift spectra were recorded by fluorescence spectro-fluorophotometer, RF-5301 PC, Shimadzu, Japan at an excitation wavelength of 350 nm and a DXR Raman Microscope, Thermo Scientific, USA, equipped with 532 nm laser as the excitation source at 6mW power respectively. The XRD patterns of as-synthesized samples were acquired by Xpert x-ray powder diffractometer (Philips PW1398) with Cu *Kα* radiation source from 20^{o} to 80^{o} (2*θ*) with a step time of 3 seconds and step size of 0.05^{o} whereas the changes in the morphology were examined by Field Emission Scanning Electron Microscope (JEOL JSM 6490-A). The variations in the oxidation states of Fe were estimated by X-ray photoelectron

spectroscopy (XPS) in the binding energy range of 0 eV to 1350 eV by X-ray Photoelectron Spectrometer (PHI 5000 Versa Probe II, ULVAC-PHI Inc., USA).

The comparison of the electrochemical properties of the as-synthesized polymorphs, in the dark and under illumination, was carried out by cyclic voltammetry (CV) and electrochemical impedance spectroscopy (EIS). For CV and EIS analysis, a VSP multi-channel potentiostat (Bio-logic Science Instrument, USA) equipped with Ec-lab software and a three-electrode system was employed, where the glassy carbon, platinum, and Ag/AgCl saturated electrodes were used as working, counter and reference electrodes, respectively. The polymorphs were coated at a surface of glassy carbon electrode (GCE) by spreading the dispersion of the ultra-sonicated dispersion in chloroform. The fitting of EIS Nyquist plots was performed by Zfit (Ec-lab software, Bio-logic Science Instruments, USA). The 0.1 M KCl solution was used as an electrolyte for all the measurements. For measurements under illumination, a 50-watt halogen lamp was used as illumination source.

The photocatalytic activity of both the polymorphs i.e. α-Fe_2O_3 and γ-Fe_2O_3 was evaluated in the exposure of the complete spectrum of sunlight (S) and visible region of sunlight (V) under identical experimental conditions. In a typical experiment, 150 ml of catalyst/substrate suspension containing 50 ppm of the substrate and 75 mg of the respective polymorph was exposed. Prior to exposure, the dark experiments were performed to establish the adsorption-desorption equilibrium. All the experiments were performed under natural sunlight illumination of $1100\pm100 \times 10^2$ lx and fixed period of the daylight. After removing the catalyst by 0.22μm disposable syringe filters, the samples drawn at regular intervals were analyzed by high-performance liquid

chromatography (HPLC, SPD-20A, Shimadzu Corporation, Japan) using methanol-water mixture (60:40 v/v) as eluent and reversed phase C18 (RP-C18) column. The mineralization of the substrates was estimated by TOC removal measured by TOC-VCPH total carbon analyzer supplied by Shimadzu Corporation, Japan. The release of ions in the solution during the photocatalytic degradation process was monitored by ion chromatograph, Dionex (ICS-5000 + EG) Eluent Generator, Thermo Scientific, USA.

3. Results and discussion

As presented in Fig. 1a, the absorption patterns of α and γ-Fe_2O_3 were recorded in a broad spectral range of 200 to 900 nm with a view including all the transition involved. Both the polymorphs adopted a similar absorption pattern and exhibited substantial absorption in 450 nm to 750 nm range. The gradually increasing absorption with the increase in the photon energy from 750 nm to 620 nm may be attributed to low energy d-d transition. The t_{2g} to e_g transitions in the 3d orbitals are well established and discussed well in the literature [50]. For both the polymorphs, beyond 620 nm towards the lower wavelength, a sharp increase in the absorption was noticed. For α-Fe_2O_3, the absorption edge appeared at ~620 nm whereas that for γ-Fe_2O_3 appeared at ~625 nm. The O^{2-} 2p orbitals constitute the valence band of Fe_2O_3 whereas the conduction band is composed of Fe^{3+} 3d orbitals. These absorption edges represent the band gap excitations in the polymorphs. The direct bandgaps of the polymorphs were evaluated by plotting $(F(R) \times h\nu)^{1/2}$ versus the photon energy (hν) where F(R) is the Kubelka-Munk transformation of the %R data. The graphical evaluation of the band edges of the Fe_2O_3 polymorphs is presented in Fig. 1b, where the extrapolation of the linear portion of the curves to the x-

axis (photon energy) resulted in the bandgaps of 2.1 eV and 2.0 eV for α- and γ-Fe_2O_3, respectively. The observed bandgap values were in accordance with the literature values [51].

The comparison of the normalized experimental PL spectra of α- and γ-Fe_2O_3 at an excitation wavelength of 350 nm is presented in Fig. 1c. The emission spectra of α- and γ-Fe_2O_3 followed the similar patterns and appeared in the form of a broadband centered at 550 and 563 nm respectively. The experimental curves were fitted to locate the actual photon energy of the emissions that arise due to the Fe^{3+} 3d to O^{2-} 2p de-excitations of the electrons. Although slightly higher, however, the observed values of ~2.23 eV and 2.13 eV were in good agreement with the literature values and also validated by the optically evaluated bandgap energies (Fig. 1a). Additionally, the significantly lower emission intensity predicted the better ability of γ-Fe_2O_3 in quenching the charge carrier recombination process than α-Fe_2O_3. As the synthesis of γ-Fe_2O_3 has been carried out by Fe^{2+} rather than Fe^{3+} ions, probably due to the fraction of Fe^{2+} ions present in the structure, the convinced defects serve as the trapping sites for the excited electrons. The comparison of the Raman spectra of the two polymorphs is presented in the inset of Fig. 1d. It is important to mention here that for both the polymorphs, even after the repeated analysis, well-resolved Raman peaks were not observed. However, the identification of the maxima was possible in the broad Raman shift patterns. The major peaks for α-Fe_2O_3 appeared at 175.34, 206.91, 251.52, 327.79, 444.36, 519.57 and 590.93 cm^{-1}. As per literature, with the minor variations, the peaks at 204.52 cm^{-1} and 519 cm^{-1} were assigned to A_{1g} mode whereas the peaks at 250.52, 322.79, 440.36 and 590.93 cm^{-1} corresponded to E_{2g} mode [52]. Compared to α-Fe_2O_3, a significant change in the peak

position was noticed for γ-Fe_2O_3 and the major peaks were observed at 180.16, 211.98, 271.76, 323.83, 380.72, 499.32 and 590.93 cm^{-1}. These peaks also correspond to the same vibrational modes as that for α-Fe_2O_3 however, depicted different rigidities of Fe-O bonds in both due to different structural arrangements. The absence of the typical peak in 660-670 cm^{-1} region completely ruled out the existence of Fe_3O_4 (magnetite) phase [52, 53].

Fig. 2 shows the comparison of the XRD patterns of α and γ polymorphs of Fe_2O_3. Both the polymorphs showed the distinct XRD patterns with visible variations. The major reflections of α-Fe_2O_3 appeared at 2θ values of 24.14º, 33.14º, 35.65º, 40.86º, 49.57º, 62.40º and 64.04º that represented the (012), (104), (110), (113), (024), (214) and (300) faces respectively, of the rhombohedral geometry (JCPDS # 33-0664) [54-56]. A crystallite size of 40.2 nm was evaluated on the basis of the most intense reflection at 33.14º. Although few reflections were common for both the polymorphs, however, the XRD pattern γ-Fe_2O_3 was distinctly different from that of α polymorph. For γ-Fe_2O_3, the foremost reflections at (220), (311), (400), (422), (511) and (440) represented the faces of the cubic structure [55-58]. A sound agreement was noticed between the experimentally observed with that of standard values (JCPDS# 39-1346) [55-58]. The application of Scherer's equation on the most intense reflection revealed a crystallite size of 31.9 nm. The sharpness of the peaks in the XRD patterns of both the polymorphs depicted the high crystallinity and phase purity of the polymorphs.

The FESEM images of α and γ polymorphs of Fe_2O_3 at 60kx, 120kx and 250kx are compared in Fig. 3a- f. For α-Fe_2O_3, the adopted synthetic route resulted in a wide particle size distribution that ranged between 30-70 nm. The bigger particles appeared to be the aggregates of the smaller particles. Interestingly, a uniformity in the shape that was

independent of the size of the particles, was witnessed. On the other hand, the adopted procedure truncated the particle size distribution of the γ-Fe_2O_3, where the particle size ranged between 10 nm to 40 nm. Additionally, various irregular morphologies with respect to the shape of the particles were also dominant. Probably, due to the magnetic nature, the aggregation of the smaller particles into larger particles was observed as the common feature.

The microstructure analysis, existence of synthesis associated defects and the phase purity of the polymorphs was further investigated by HRTEM analysis. The HRTEM images of the α-Fe_2O_3 are presented in Fig. 4. The images at different resolutions (Fig. 4a and b) clearly revealed the size-independent rhombohedral geometry of the particles with sharp edges. The focusing at high magnification indicated more than one lattice arrangement of atoms in a single crystal. The isolated fringe patterns with the d-spacing of 0.252 nm and 0.283 nm are presented in Fig. 4c and d, respectively. The major phase with the d-spacing of 0.252 nm represented the dominant rhombohedral geometry whereas the lattice pattern with the spacing of 0.283 nm represented the minor defect phase in the crystal. The observation confirmed the non-stoichiometric defective structure of the synthesized α-Fe_2O_3. The SAED patterns of the isolated atomic arrangements, Fig.4e, and f also verified the major and defect phases in the synthesized powder. The HRTEM images of the γ-Fe_2O_3 are presented in Fig. 5. The irregular shaped particles of γ-Fe_2O_3 as estimated by FESEM, are observable in the TEM image (Fig. 5a). The reflections in the SAED pattern, as presented in Fig. 5b, were consistent with the XRD sequence of cubic γ-Fe_2O_3. The phase purity of the synthesized powder was assessed by focusing the single crystals at two different locations. Both the images, as

presented in Fig.5c and d, revealed the existence of the similar atomic layer arrangements with the d-spacing of 0.283 nm.

The assessment of the oxidation states and chemical environment of Fe in α- and γ- polymorphs of Fe_2O_3 was carried out by XPS analysis. The wide-angle survey scans of both the polymorphs in the binding energy range of 0 eV to 1350 eV are compared in Fig. 6a, where the peaks corresponding to Fe, O, and C are observable. The characteristic C 1s peak at ~284.08 eV authenticated the validity of the adopted procedure. The comparison of the high-resolution Fe 2p peaks of both the polymorphs is presented in Fig. 6b. Apparently, both the peaks were of asymmetric nature that indicated the existence of either multiple oxidation states or the varying chemical environment of Fe^{3+} in the samples. For α-Fe_2O_3, the Fe $2p_{3/2}$ and Fe $2p_{1/2}$ peaks appeared at ~710.88 eV and ~724.98 eV respectively, whereas for γ-Fe_2O_3 the same were observed at ~711.68 eV and ~725.18 eV. The intensity of the distinct shakeup satellite at ~719 eV was significantly higher for α- as compared to γ- polymorph. The observed shapes and the positions of the Fe 2p peaks were in accordance with the previous studies [59, 60]. The high-resolution O 1s peaks are compared in Fig. 6c, where the dominant peaks were observed in ~530 eV and ~532 eV region that were assigned to skeletal and surface oxygen respectively. The intensity of the peak corresponding to the surface oxygen was significantly higher for γ as compared to α-Fe_2O_3 that depicted the higher tendency of γ-Fe_2O_3 towards surface O-H formation. The observation was in compliance with that reported earlier [61, 62]. The deconvoluted, fitted Fe 2p peaks of both the polymorphs are compared in Fig. 6d and e, respectively. The careful analysis and fitting revealed the splitting of both Fe $2p_{3/2}$ and Fe $2p_{1/2}$ peaks due to the changed chemical environment rather than varying oxidation states.

For α-Fe_2O_3, the intensity of the peak due to the skeletal Fe^{3+} was significantly higher than that of surface Fe^{3+} whereas the increased intensity of the surface Fe^{3+} was witnessed for γ-polymorph. The observation was in agreement with the analysis of O 1s peaks for both the polymorphs.

Prior to actual photocatalytic experiments, the estimation of the adsorption of 2-NP revealed a significantly high adsorption on α-Fe_2O_3 (~24%) as compared to that on γ-Fe_2O_3 (~9%) that depicted the availability of a sufficiently higher number of active sites at the surface of α- as compared to γ- polymorph. The comparison of the time-scale percentage degradation of 2-nitrophenol (2-NP) on both the polymorphs, as extracted from the HPLC degradation profiles, in the complete spectrum and visible region sunlight exposure is presented in Fig. 7a. The α-Fe_2O_3 degraded ~36% in the initial 30 minutes of exposure, whereas γ-Fe_2O_3 removed only ~23% of 2-NP in the same period. Both the polymorphs showed sluggish activity in the initial 60 minutes of exposure whereas a significant improvement was noticed afterward. Although the activity of γ-Fe_2O_3 for the removal of 2-NP was slightly lower than that of α-Fe_2O_3, however, both the polymorphs managed to degrade ≥ 99% of 2-NP in 300 minutes of sunlight exposure. Although much lower than that in the complete spectrum, a consistent degradation of 2-NP was noticed on both the polymorphs in the visible region sunlight exposure. Compared to ~67% and ~53% removal in 90 minutes of complete spectrum, ~40% and ~31% of 2-NP was removed over α and γ-Fe_2O_3 respectively, in the visible region exposure, in the same period. After 300 minutes of exposure, the α and γ polymorphs removed 74% and 70% of 2-NP respectively. The validation of the Langmuir-Hinshelwood kinetic model for pseudo-first order reactions for the removal of phenols was evaluated by plotting the

$\ln(C_o/C)$ versus the sunlight (complete spectrum/visible) exposure time and presented in Fig. 7b. It was noticed that the degradation process in the complete spectrum sunlight exposure completely deviates from the kinetic model for both the polymorphs. The rate of the degradation process increased gradually in the initial 90 minutes of exposure followed by an abrupt increase afterward. On the other hand, a sound validation was experiential for both the catalysts in the exposure of the visible region of the sunlight where a linear increase in the rate of degradation was witnessed with the increased exposure time. In the visible region exposure both the polymorphs degraded 2-NP almost at the same rate and the observed rate constant was ~3.5×10^{-3} min^{-1}.

As presented in Fig. 7c, compared to ~24% for 2-NP, the adsorption of 2-chlorophenol (2-CP) on α-Fe_2O_3 was substantially lower i.e. ~14%, whereas 1% higher than 2-NP on γ-Fe_2O_3. As compared to 2-NP, the removal of 2-CP was significantly lower on both the polymorphs. In the initial 60 minutes of exposure, ~34% and ~32% of 2-CP compared to ~47% and ~38% of 2-NP was degraded in the presence of α and γ polymorphs. Interestingly, in case of 2-CP, both the polymorphs performed almost equally in the initial 120 minutes of sunlight exposure however, α-Fe_2O_3 showed higher activity afterward. Both the polymorphs removed ≥ 99% of 2-CP in 300 minutes of exposure. For the removal of 2-CP in visible region exposure, the behavior of both the polymorphs was similar to that for 2-NP degradation, however, the activity of α-Fe_2O_3 was marginally higher than that of γ-Fe_2O_3. After the prescribed time of 300 minutes of visible light exposure, ~82% and ~76% of 2-CP was removed by α and γ polymorph respectively. The graphical evaluation of the rates of the degradation of 2-CP is presented in Fig. 7d, where a situation similar to that of 2-NP degradation was witnessed. The

Langmuir-Hinshelwood kinetic model was completely violated for the degradation of 2-CP in the complete spectrum sunlight exposure whereas, validated in the exposure to the visible region exposure. The evaluated rate constants for the removal of 2-CP were ~4.7 $\times 10^{-3}$ min^{-1} and ~4 $\times 10^{-3}$ min^{-1} for α- and γ- polymorph of Fe_2O_3.

The comparison of the simultaneous TOC removal (ppm) during the degradation of 2-NP as a function of the complete spectrum and visible light exposure time over α and γ-Fe_2O_3 is presented in Fig. 8a. Starting from ~26 ppm in the dark, α- and γ-Fe_2O_3 reduced the TOC of the system to 1.4 ppm and 2.01 ppm respectively in 300 minutes of complete spectrum sunlight exposure. The concurrent decrease in the TOC clearly indicated that the degradation and TOC removal process proceeds simultaneously. The TOC removal during the degradation of 2-NP in the exposure of visible region was significantly lower (≤ 40% for both the polymorphs) than that observed for complete spectrum sunlight exposure. The graphical evaluation of the rate constants for the TOC removal for both the polymorphs under the preset exposure conditions is presented in Fig. 8b. A mild variation from the Langmuir-Hinshelwood kinetics was witnessed for the TOC removal process for both the polymorphs. The rate of TOC removal in the visible region was significantly lower than that observed for complete spectrum sunlight exposure. The observed rate constants for the TOC removal in visible light exposure were ~2.2 $\times 10^{-3}$ min^{-1} and ~1.9 $\times 10^{-3}$ min^{-1} for α- and γ- polymorph, respectively. As presented in Fig. 8c, compared to 2-NP, the TOC removal for 2-CP was rather slow and a low TOC removal was noticed at the completion of 300 minutes of the exposure time. The graphical evaluation of the rate constants (Fig. 8d) also revealed low rates of TOC removal for both the polymorphs during the degradation of 2-CP. Interestingly, contrary

to that observed in the 2-NP substrate degradation and mineralization, for 2-CP, a sound corroboration of Langmuir-Hinshelwood kinetics was witnessed for TOC removal process for both the polymorphs. The evaluated rate constants for the TOC removal in the presence of for α and γ polymorphs were ~6.4×10^{-3} min^{-1} and ~5.6×10^{-3} min^{-1} respectively, which were substantially lower than that of 2-NP. The rate constants for TOC removal in the visible region of sunlight during the degradation of 2-CP were also lower than that observed for 2-NP however, the Langmuir-Hinshelwood kinetic model was also validated.

From the results presented above, the major findings can be summarized as follows:

- The initially low degradation of phenolic substrates followed by a sharp increase, in the complete spectrum sunlight compared to visible region exposure, depicted the probable changes induced by UV photons that enhance the yield of reactive oxygen species (ROS) in the system.
- Although occur simultaneously, the rapid degradation compared to mineralization revealed the degradation as priority process.
- The substrates are not mineralized directly followed by degradation rather intermediates are formed.
- The comparable rates of degradation whereas the low rate of mineralization of 2-CP compared to that of 2-NP, indicate that the degradation of 2-NP and 2-CP results in the formation of intermediates that differ both in chemical nature and stability.

Both α- and γ- polymorphs of Fe_2O_3 are the n-type semiconductors and differ only in the structural arrangement of Fe^{3+} and O^{2-} entities in the crystal structure that impart rhombohedral and cubic geometry, respectively. As the nature and population of the ROS generated, with the absorption of the photons, in the photocatalytic system, is dependent on the electrochemical potential associated with the band edges, therefore the same was evaluated theoretically by applying the procedure detailed in equations 1 and 2 below [63, 64]:

$$E_v = -\chi - 0.5E_g \quad (1)$$

$$E_c = -\chi + 0.5E_g \quad (2)$$

Where χ is the electronegativity and E_g is the bandgap excitation energy. The acquired values of E_v and E_c against the absolute vacuum scale (AVS) can be transformed to that against the normal hydrogen electrode (NHE) by using the relation below in equation 3:

$$E(NHE) = -E(AVS) - 4.5 \quad (3)$$

Therefore, using the electronegativity value of 5.88, for Fe_2O_3, from the literature [51] and the experimentally evaluated band edge positions of 2.1 eV and 2.0 eV for α and γ- polymorphs, the evaluated potentials of the valence and the conduction bands were +2.43 V (E_v, α-Fe_2O_3), +2.38 V (E_v, γ-Fe_2O_3), +0.33 V (E_c, α-Fe_2O_3) and +0.38 V (E_c, γ-Fe_2O_3). The estimated values for α-Fe_2O_3 were in sound agreement with the experimentally determined values [65].

In the aqueous photocatalytic system, the hydroxyl and superoxide radicals, jointly termed as reactive oxygen species (ROS), are regarded as the "primary oxidants" that are produced as a result of water oxidation and reduction of adsorbed or dissolved

oxygen. The further interaction of primary ROS other and molecular, radical and ionic species presents in the system produce a number or long or short-lived "secondary ROS". The generation and population of the primary ROS are regulated by the electrochemical potential of the band edges of the photocatalyst under illumination. The generation of primary ROS is outlined in the equations 4 and 5 below [66].

$$H_2O + h_{vb}^{+} \rightarrow H_2O^{+} \rightarrow HO^{\bullet} + H^{+} (E_v \geq +1.23V) \quad (4)$$

$$O_2 + e_{cb}^{-} \rightarrow O^{\bullet -} (E_c \leq -0.28V) \quad (5)$$

Based on the above equations, the analysis of the evaluated potentials of the band edges revealed the suitability of E_v of both the polymorphs for the oxidation of water, however, the positive value of E_c completely ruled out the possibility of the formation of superoxide anion radicals. Therefore, for both the polymorphs, it can be anticipated that the degradation of the phenolic substrates is carried out by the interaction of the hydroxyl radicals. To verify this assumption, the time-scale HPLC profiles for the degradation 2-NP and 2-CP over α and γ polymorphs in full spectrum sunlight exposure were plotted and presented in Fig. 9a-d, where the adsorption of the substrates on the catalysts in the dark, the progressive decrease in the concentration of phenolic substrates and the formation of intermediates (represented by the blue arrow) is observable. Although the concentration of both the substrates was 50 ppm, however, compared to 2-CP, a significantly intense peak response of 2-NP, at the detector wavelength of 254 nm, was noticed. Additionally, as expected, the appearance of the intermediates at diverse retention times for both the substrates depicted their dissimilar chemical nature.

Interestingly, the observed patterns of degradation of the single substrate either 2-NP or 2-CP on both the polymorphs were indistinguishable. The identification of intermediates for both the substrates by HPLC (based on the availability of reference materials) and GCMS revealed hydroxyl groups substituted intermediates. In the GCMS analysis of selected samples, besides the hydroxyl group substituted intermediates a variety of oxygenated aliphatic intermediates that included alcohols, esters etc. In the exposure of the visible region of sunlight, along with the minute fraction of aliphatic oxygenates, the majority intermediates were hydroxyl substituted intermediates. The analysis and comparison of the HPLC profiles (Fig. 9) also revealed the formation of "hard" intermediates in the degradation of 2-CP that resist mineralization process whereas "soft" intermediates are formed during the degradation of 2-NP and mineralized with ease.

Compared to visible region, in the complete spectrum sunlight exposure, the linear rate of degradation initially followed by an abrupt increase afterward along with the presence of aliphatic oxygenates as intermediates in the degradation of both the substrates over α and γ polymorphs unveiled the significant role of just 3-5% portion of UV photons in natural sunlight. It was anticipated that the absorption of the UV photons, having significantly higher energy than the bandgap of both the polymorphs, induces structural changes at the surface that facilitates the quenching of excitons recombination for a prolonged lifetime, improve transfer-ability and enhanced activity. Probably, the absorption of the energetic UV photons ($E_p >> E_g$) leads to the estrangement of Fe^{3+}-O bond pledging the formation of Fe^{3+} based surface defects that act as a trap and transfer centers for the excited electrons.

To verify the assumption of induction of surface defects by UV photons, the unexposed and pre-sunlight exposed α- and γ-Fe_2O_3 were subjected to electrochemical analysis by cyclic voltammetry (CV) and electrochemical impedance spectroscopy (EIS) both in the dark and under illumination. To rule out the effect of pH and the possible interaction or interference from the electrolyte, 0.1M KCl was used as the electrolyte at neutral pH. The CV's were recorded in a broader potential range of -1.5 to +1.5 V. The comparison of the CV patterns of unexposed α-Fe_2O_3, in dark and under illumination, is presented in Fig. 10a. In spite of discussing all the peaks that appeared in the CV patterns under our experimental conditions, we concentrated on the peaks that appeared under illumination or that were already present in the dark and their magnitude was enhanced. For α-Fe_2O_3 (unexposed), two anodic (oxidation) peaks at -0.24 V and +0.17 V were visible in the dark. There was no change in the intensity of the peak at -0.24 V, in the dark and under illumination, whereas the intensity of the peak at +0.17 V was significantly enhanced under the exposure and attributed to the oxidation of surface Fe^{2+} to Fe^{3+} species. The appearance of the same in the dark verified the pre-existence of Fe^{2+} based defects in α-Fe_2O_3 however, the process of formation of these defects is escalated with the interaction of UV photons of the complete spectrum sunlight that results in the enhancement of oxidation peak current. A similar behavior was observed for unexposed and pre-exposed γ-Fe_2O_3 (Fig. 10b), however, the intensity of the oxidation peak at +0.17 V was significantly lower than that of α-Fe_2O_3 under both exposure conditions that proved its superior stability under UV exposure. Additionally, the higher background current for γ-Fe_2O_3 depicted its better charge transfer-ability than α-Fe_2O_3. The stability of both the polymorphs was further investigated by recording the CV patterns of pre-

exposed polymorphs. The comparisons of the CV patterns of the pre-exposed (prepared by exposing to complete spectrum sunlight for three hours) α and γ-Fe_2O_3, in the dark and under illumination, are presented in Fig. 10c and d, respectively. The concurrent appearance of the oxidation peak at +0.17 V for pre-exposed α-Fe_2O_3 under exposure revealed the susceptibility of its surface for further formation of Fe^{2+} based defects with the interaction of UV photons. Interestingly, no such pattern was witnessed for γ-Fe_2O_3 after repeated scans that validated the saturation of Fe^{2+} defects at the surface and protracted stability. The study also highlighted the practicality of cyclic voltammetry for the identification of surface defects and evaluation of the stability of the materials [67].

The EIS spectra provide a deep insight to the resistance offered by the material to the transfer of electrons to the electrode surface and separation of the electron-hole pair [68, 69]. The comparison of the EIS Nyquist plots of the exposed and pre-exposed α-Fe_2O_3, under illumination, is presented in Fig. 11a and b, where compared to unexposed, a decreased resistance to the electron transfer was noticed for pre-exposed α-Fe_2O_3 that highlighted the significance of Fe^{2+} based surface defects for trapping and transfer of excited electrons. The reduced diameter of the high-frequency semicircular portion in the EIS spectra of pre-exposed compared to exposed α-Fe_2O_3 depicted the better transportability of excitons generated under illumination. A similar picture was portrayed in the low-frequency linear region (presented in Fig. 11c and d). The EIS behavior of pre- and unexposed γ-Fe_2O_3 was identical to that of α-Fe_2O_3 however, pre-exposed γ-Fe_2O_3 exhibited better electron transport capability as compared to pre-exposed α-Fe_2O_3. The better electrical conductance of the pre-exposed polymorphs may be attributed the electron capture and transfer capacity of Fe^{2+} surface states.

The effects of the UV photons induced Fe^{2+} based surface defects on the adsorption and photocatalytic activity was evaluated in the dark and visible region of sunlight exposure using 2-NP as substrate. A considerable increase in the adsorption of the 2-NP on both the pre-exposed polymorphs was noticed. The comparison of the adsorption and degradation of 2-NP in the presence of pre- and unexposed polymorphs is presented in Fig. 12. A substantial increase in the adsorption of the 2-NP on both the pre-exposed polymorphs was noticed. Compared to unexposed α-Fe_2O_3 (~24%) and γ-Fe_2O_3 (~9%), ~31% and ~21% of 2-NP was adsorbed on pre-exposed α and γ polymorph of Fe_2O_3 respectively. The pre-exposed polymorphs also exhibited substantially high activity for the degradation of 2-NP as an overall increase of ~20% was observed for both the polymorphs. These observations suggested that the surface presence of defects enhance the generation of reactive oxygen species (ROS) either by enhancing the water oxidation process or the reduction of adsorbed/dissolved oxygen. Hence it can be presumed that the surface defects serve as excited electrons trapping and transfer center thus extending the life-time of excited states and promoting the transfer of excitons.

To verify the assumption of the formation of sunlight-induced surface defects, the photocatalytic activity of pre-exposed and unexposed α-Fe_2O_3 and γ-Fe_2O_3 was examined for the degradation of 2-NP in the exposure of the visible region of sunlight. For use in the experiment, both the powders were exposed to the natural sunlight in the aqueous medium for three hours. The comparison of the activity of the pre-exposed and unexposed α-Fe_2O_3 and γ-Fe_2O_3 for the removal of 2-NP is presented in Fig. 12. Prior to exposure, the evaluation of the adsorption of the substrate at the surface of the powders revealed an enhanced adsorption on the pre-exposed samples of both the powders as

compared to the pristine samples. The observation led to the inference that the interaction of the UV portion (3-5%) of the natural sunlight, as no significant change in the adsorption and activity was witnessed for the samples exposed to the visible region of the sunlight, generate the active sites that facilitate the enhanced adsorption of the substrate. The increased adsorption of varying magnitude further elaborated that the defects are generated both powders however, a lower magnitude was observed for γ-Fe_2O_3 as compared to α-Fe_2O_3. As both the powders are the short bandgap semiconductors, it might be presumed that the interaction of high energy UV photons generate the surface defects. A more than ~20% increase in the overall activity of the pre-exposed samples revealed that the generated active sites not only serve as the adsorption sites but also serve as a trap and transfer centers for the excited electrons that in turns enhance the photocatalytic activity of the powders in the visible regions. It is important to mention here that no significant effect on the magnetic retrievability of γ-Fe_2O_3 was noticed. Additionally, the analysis of the solution for the estimation of Fe based entities in the solution revealed the restriction of the defects without the photocorrosion.

4. Conclusions

The study revealed that both α-Fe_2O_3 and γ-Fe_2O_3 possess the substantial activity in the visible region and complete spectrum sunlight exposure. The examination of the degradation products revealed that both the powders generate highly oxidizing radicals that play a vital role in the degradation/mineralization process. The nature of the degradation products is strongly dependent on the nature of the substituents present. The electrochemical measurements revealed better stability of γ-Fe_2O_3 as compared to α-

Fe_2O_3. Both the materials are prone to surface defects after absorbing the high energy UV photons of the sunlight. The defects play facilitating role in enhancing the photocatalytic activity. Although the photocatalytic activity of γ-Fe_2O_3 was slightly lower than that of α-Fe_2O_3 however, better chemical stability and magnetic nature make it a better choice for photocatalytic applications.

Acknowledgements

A. Hameed and M. Aslam are thankful to Center of Excellence in Environmental Studies, King Abdulaziz University and Ministry of Higher Education (MoHE), KSA, for support.

References

1. M.D. Hernández-Alonso, F. Fresno, S. Suárez, J.M. Coronado, Development of alternative photocatalysts to TiO_2: Challenges and opportunities, Energy Environ. Sci. 2 (2009) 1231-1257.
2. J. Zeng, T. Song, M. Lv, T. Wang, J. Qin, H. Zeng, Plasmonic photocatalyst Au/g-C_3N_4/$NiFe_2O_4$ nanocomposites for enhanced visible-light-driven photocatalytic hydrogen evolution, RSC Adv. 6 (2016) 54964-54975.
3. A.D. Paola, E. García-López, G. Marcì, L. Palmisano, A survey of photocatalytic materials for environmental remediation, J. Hazard. Mater. 211-212 (2012) 3-29.
4. A. Hameed, M. Aslam, I.M.I. Ismail, S. Chandrasekaran, M.W. Kadi, M.A. Gondal, Sunlight assisted photocatalytic mineralization of nitrophenol isomers over W^{6+} impregnated ZnO, Appl. Catal. B: Environ. 160-161 (2014) 227-239.
5. A. Fujishima, X. Zhang, D.A. Tryk, TiO_2 photocatalysis and related surface phenomena, Surf. Sci. Rep. 63 (2008) 515-582.

6. A. Hameed, M. Aslam, I.M.I. Ismail, N. Salah, P. Fornasiero, Sunlight induced formation of surface Bi_2O_{4-x}-Bi_2O_3 nanocomposite during the photocatalytic mineralization of 2-chloro and 2-nitrophenol, Appl. Catal., B: Environ. 163 (2015) 444-451.

7. K. Nakata, A. Fujishima, TiO_2 photocatalysis: design and applications, J. Photochem. Photobiol. C: Photochem. Rev. 13 (2012) 169-189.

8. A.L. Linsebigler, G. Lu, J.T. Yates, Photocatalysis on TiO_2 surfaces: principles, mechanisms, and selected results, Chem. Rev. 95 (1995) 735-758.

9. J. Schneider, M. Matsuoka, M. Takeuchi, J. Zhang, Y. Horiuchi, M. Anpo, D.W. Bahnemann, Understanding TiO_2 photocatalysis: mechanisms and materials, Chem. Rev. 114 (2014) 9919-9986.

10. S. Rehman, R. Ullah, A.M. Butt, N.D. Gohar, Strategies of making TiO_2 and ZnO visible light active, J. Hazard. Mater. 170 (2009) 560-569.

11. M.T. Qamar, M. Aslam, Z.A. Rehan, M.T. Soomro, J.M. Basahi, I.M.I. Ismail, T. Almeelbi, A. Hameed, The influence of p-type Mn_3O_4 nanostructures on the photocatalytic activity of ZnO for the removal of bromo and chlorophenol in natural sunlight exposure, Appl. Catal. B: Environ. 201 (2017) 105-118.

12. M. Aslam, I.M.I. Ismail, S. Chandrasekaran, A. Hameed, Morphology-controlled bulk synthesis of disc-shaped WO_3 powder and evaluation of its photocatalytic activity for the degradation of phenols, J Hazard Mater. 276 (2014) 120-128.

13. M. Aslam, I.M.I. Ismail, S. Chandrasekaran, T. Almeelbi, A. Hameed, The suitability of Ce^{3+}-modified ZnO photocatalyst for the mineralization of

monochlorophenol isomers in sunlight exposure, RSC Adv. 4 (2014) 49347-49359.

14. M.T. Qamar, M. Aslam, Z.A. Rehan, M.T. Soomro, J.M. Basahi, I.M.I. Ismail, A. Hameed, The effect of Fe^{3+} based visible light receptive interfacial phases on the photocatalytic activity of ZnO for the removal of 2,4-dichlorophenoxy acetic acid in natural sunlight exposure, Sep. Purif. Technol. 172 (2017) 512-528.

15. S.W. Cao, Y.J. Zhu, Hierarchically Nanostructured α-Fe_2O_3 Hollow Spheres: Preparation, Growth Mechanism, Photocatalytic Property, and Application in Water Treatment, J. Phys. Chem. C 112 (2008) 6253-6257.

16. C. Kormann, D.W. Bahnemann, M.R. Hoffmann, Environmental photochemistry: Is iron oxide (hematite) an active photocatalyst? A comparative study: α-Fe_2O_3, ZnO, TiO_2, J. Photochem. Photobiol. A: Chem. 48 (1989) 161-169.

17. S.K. Apte, S.D. Naik, R.S. Sonawane, B.B. Kale, J.O. Baeg, Synthesis of Nanosize-Necked Structure α- and γ-Fe_2O_3 and its Photocatalytic Activity, J. Am. Ceram. Soc. 90 (2007) 412-414.

18. T. Song, P. Zhang, J. Zeng, T. Wang, A. Ali, H. Zeng, Boosting the photocatalytic H_2 evolution activity of Fe_2O_3 polymorphs (α-, γ- and β-Fe_2O_3) by fullerene [C_{60}]-modification and dye-sensitization under visible light irradiation, RSC Adv. 7 (2017) 29184-29192.

19. S. Cao, F. Kang, P. Li, R. Chen, H. Liu, Y. Wei, Photo assisted hetero-Fenton degradation mechanism of Acid Blue 74 by a γ-Fe_2O_3 catalyst, RSC Adv. 5 (2015) 66231-66238.

20. M. Mishra, D.M. Chun, α-Fe_2O_3 as a photocatalytic material: A review, Appl. Catal. A: Gen. 498 (2015) 126-141.

21. F. Qian, H. Wang, Y. Ling, G. Wang, M.P. Thelen, Y. Li, Photoenhanced electrochemical interaction between *Shewanella* and a hematite nanowire photoanode, Nano Lett. 14 (2014) 3688-3693.

22. B.M. Klahr, A.B.F. Martinson, T.W. Hamann, Photoelectrochemical investigation of ultrathin film iron oxide solar cells prepared by atomic layer deposition, Langmuir 27 (2011) 461-468.

23. L. Cao, Y. Zeng, Z. Ye, Z. Wang, Y. Zhang, L. Zhao, C. Li, C. Zhang, Preparation of 2D α-Fe_2O_3 platelets via hydrothermal heterogeneous growth approach and their magnetic property studies, New J. Chem. 41 (2017) 6436-6444.

24. W. Sun, Q. Meng, L. Jing, D. Liu, Y. Cao, Facile synthesis of surface-modified nanosized α-Fe_2O_3 as efficient visible photocatalysts and mechanism insight, J. Phys. Chem. C 117 (2013) 1358-1365.

25. P. Wang, D. Wang, J. Lin, X. Li, C. Peng, X. Gao, Q. Huang, J. Wang, H. Xu, C. Fan, Lattice defect-enhanced hydrogen production in nanostructured hematite-based photoelectrochemical device, ACS Appl. Mater. Interfaces 4 (2012) 2295-2302.

26. T. Song, J. Huo, T. Liao, J. Zeng, J. Qin, H. Zeng, Fullerene [C60] modified $Cr_{2-x}Fe_xO_3$ nanocomposites for enhanced photocatalytic activity under visible light irradiation, Chem. Eng. J. 287 (2016) 359-366.

27. J. Li, N. Wu, Semiconductor-based photocatalysts and photoelectrochemical cells for solar fuel generation: A review, Catal. Sci. Technol. 5 (2015) 1360-1384.

28. Z. Sun, H. Yuan, Z. Liu, B. Han, X. Zhang, A highly efficient chemical sensor material for H_2S: α-Fe_2O_3 nanotubes fabricated using carbon nanotube templates, Adv. Mater. 17 (200) 2993-2997.

29. M.P. Morales, S. Veintemillas-Verdaguer, M.I. Montero, C.J. Serna, Surface and internal spin canting in γ-Fe_2O_3 nanoparticles, Chem. Mater. 11 (1999) 3058-3064.

30. J. Govan, Y.K. Gun'ko, Recent advances in the application of magnetic nanoparticles as a support for homogeneous catalysts, Nanomaterials 4 (2014) 222-241.

31. T. Mitsudome, K. Kaneda, Advanced core–shell nanoparticle catalysts for efficient organic transformations, Chem. Cat. Chem. 5 (2013) 1681-1691.

32. T. Cheng, D. Zhang, H. Li, G. Liu, Magnetically recoverable nanoparticles as efficient catalysts for organic transformations in aqueous medium, Green Chem.16 (2014) 3401-3427.

33. Y. Xu, S. Huang, M. Xie, Y. Li, L. Jing, H. Xu, Core-shell magnetic Ag/AgCl@Fe_2O_3 photocatalysts with enhanced photoactivity for eliminating bisphenol A and microbial contamination, New J. Chem. 40 (2016) 3413-3422.

34. J. Zeng, W. Zeng, H. Zeng, In situ plasmonic Au nanoparticle anchored nickel ferrite: An efficient plasmonic photocatalyst for fluorescein-sensitized hydrogen evolution under visible light irradiation, J. Solid State Chem. 253 (2017) 294-304.

35. Y. Yao, F. Lu, Y. Zhu, F. Wei, X. Liu, C. Lian, S. Wang, Magnetic core-shell $CuFe_2O_4$@C_3N_4 hybrids for visible light photocatalysis of Orange II, J. Hazard. Mater. 297 (2015) 224-233.

36. H. Wang, X. Fei, L. Wang, Y. Li, S. Xu, Magnetically separable iron oxide nanostructures-TiO_2 nanofibers hierarchical heterostructures: Controlled fabrication and photocatalytic activity, New J. Chem. 35 (2011) 1795-1802.

37. Y. Xu, S. Huang, M. Xie, Y. Li, H. Xu, L. Huang, Q. Zhang, H. Li, Magnetically separable Fe_2O_3/g-C_3N_4 catalyst with enhanced photocatalytic activity, RSC Adv. 5 (2015) 95727-95735.

38. H. Zhao, L. Zhang, X. Gu, S. Li, B. Li, H. Wang, Fe_2O_3-AgBr nonwoven cloth with hierarchical nanostructures as efficient and easily recyclable macroscale photocatalysts, RSC Adv. 5 (2015) 10951-10959.

39. A. Banisharif, A.A. Khodadadi, Y. Mortazavi, A.A. Firooz, J. Beheshtian, S. Agah, S. Menbari, Highly active Fe_2O_3-doped TiO_2 photocatalyst for degradation of trichloroethylene in air under UV and visible light irradiation: experimental and computational studies, Appl. Catal. B: Environ. 165 (2015) 209-221.

40. K. Yao, P. Basnet, H. Sessions, G.K. Larsen, S.E.H. Murph, Y. Zhao, Fe_2O_3-TiO_2 core-shell nanorod arrays for visible light photocatalytic applications, Catal. Today 270 (2016) 51-58.

41. N. Abbas, G.N. Shao, M.S. Haider, S.M. Imran, S.S. Park, H.T. Kim, Sol–gel synthesis of TiO_2-Fe_2O_3 systems: Effects of Fe_2O_3 content and their photocatalytic properties, J. Ind. Eng. Chem. 39 (2016) 112-120.

42. J. Xie, Z. Zhou, Y. Lian, Y. Hao, P. Li, Y. Wei, Synthesis of α-Fe_2O_3/ZnO composites for photocatalytic degradation of pentachlorophenol under UV-vis light irradiation, Ceram. Int. 41 (2015) 2622-2625.

43. W. Wu, S. Zhang, X. Xiao, J. Zhou, F. Ren, L. Sun, C. Jiang, Controllable synthesis, magnetic properties, and enhanced photocatalytic activity of spindle like mesoporous α-Fe_2O_3/ZnO core-shell heterostructures, ACS Appl. Mater. Interfaces 4 (2012) 3602-3609.

44. N. Ferroudj, J. Nzimoto, A. Davidson, D. Talbot, E. Briot, V. Dupuis, A. Bée, M.S. Medjram, S. Abramson, Maghemite nanoparticles and maghemite/silica nanocomposite microspheres as magnetic Fenton catalysts for the removal of water pollutants, Appl. Catal. B: Environ. 136-137 (2013) 9-18.

45. M.T. Qamar, M. Aslam, I.M.I. Ismail, N. Salah, A. Hameed, The assessment of the photocatalytic activity of magnetically retrievable ZnO coated γ-Fe_2O_3 in sunlight exposure, Chem. Eng. J. 283 (2016) 656-667.

46. N. Kaur, S.K. Shahi, V. Singh, Synthesis, characterization and photocatalytic activity of magnetically separable γ-Fe_2O_3/N,Fe codoped TiO_2 heterojunction for degradation of Reactive Blue 4 dye, RSC Adv. 5 (2015) 61623-61630.

47. Y. Liu, L. Yu, Y. Hu, C. Guo, X. Wen, D. Lou, A magnetically separable photocatalyst based on nest-like γ-Fe_2O_3/ZnO double-shelled hollow structures with enhanced photocatalytic activity, Nanoscale 4 (2012) 183-187.

48. V. Belessi, D. Lambropoulou, I. Konstantinou, R. Zboril, J. Tucek, D. Jancik, Structure and photocatalytic performance of magnetically separable titania photocatalysts for the degradation of propachlor, Appl. Catal. B: Environ. 87 (2009) 181-189.

49. S. Ye, L.G. Qiu, Y.P. Yuan, Y.J. Zhu, J. Xia, J.F. Zhu, Facile fabrication of magnetically separable graphitic carbon nitride photocatalysts with enhanced photocatalytic activity under visible light, J. Mater. Chem. A 1 (2013) 2929-3188.

50. M. Catti, G. Valerio, R. Dovesi, Theoretical study of electronic, magnetic, and structural properties of α-Fe_2O_3 (hematite), Phys. Rev. B 51(1995) 7441-7450.

51. Y. Xu, M.A.A. Schoonen, The absolute energy positions of conduction and valence bands of selected semiconducting minerals, Am. Mineral. 85 (2000) 543-556.

52. Q. Wei, Z. Li, Z. Zhang, Q. Zhou, Facile synthesis of α-Fe_2O_3 nanostructured films with controlled morphology, Mater. Trans. 50 (2009) 1351-1354.

53. N.D. Phu1, D.T. Ngo, L.H. Hoang, N.H. Luong, N. Chau, N.H. Hai, Crystallization process and magnetic properties of amorphous iron oxide nanoparticles, J. Phys. D: Appl. Phys. 44 (2011) 345002.

54. M. Aslam, M.T. Soomro, I.M.I. Ismail, H.A. Qari, M.A. Gondal, A. Hameed, The facile synthesis, characterization and evaluation of photocatalytic activity of bimetallic $FeBiO_3$ in natural sunlight exposure, RSC Adv. 5 (2015) 102663-102673.

55. H. Cui, Y. Liu, W. Ren, Structure switch between α-Fe_2O_3, γ-Fe_2O_3 and Fe_3O_4 during the large scale and low temperature sol-gel synthesis of nearly monodispersed iron oxide nanoparticles, Adv. Powder Technol. 24 (2013) 93-97.

56. X. Zhang, Y. Niu, X. Meng, Y. Li, J. Zhao, Structural evolution and characteristics of the phase transformations between α-Fe_2O_3, Fe_3O_4 and γ-Fe_2O_3 nanoparticles under reducing and oxidizing atmospheres, CrystEngComm 15 (2013) 8166-8172.

57. S. Liu, K. Yao, L.H. Fu, M.G. Ma, Selective synthesis of Fe_3O_4, γ-Fe_2O_3, and α-Fe_2O_3 using cellulose-based composites as precursors, RSC Adv. 6 (2016) 2135-2140.

58. D. Cao, H. Li, L. Pan, J. Li, X. Wang, P. Jing, X. Cheng, W. Wang, J. Wang, Q. Liu, High saturation magnetization of γ-Fe_2O_3 nano-particles by a facile one-step synthesis approach, Sci. Rep. 6 (2016) 32360.

59. M. Aronniemi, J. Sainio, J. Lahtinen, Chemical state quantification of iron and chromium oxides using XPS: the effect of the background subtraction method, Surf. Sci. 578 (2005) 108-123.

60. A. Wang, H. Yang, T. Song, Q. Sun, H. Liu, T. Wang, H. Zeng, Plasmon mediated Fe–O in an octahedral site of cuprospinel by Cu NPs for photocatalytic hydrogen evolution, Nanoscale 9 (2017) 15760-15765.

61. S.S. Li, W.J. Li, T.J. Jiang, Z.G. Liu, X. Chen, H.P. Cong, J.H. Liu, Y.Y. Huang, L.N. Li, X.J. Huang, Iron oxide with different crystal phases (α- and γ-Fe_2O_3) in electroanalysis and ultrasensitive and selective detection of lead(II): An advancing approach using XPS and EXAFS, Anal. Chem. 88 (2016) 906-914.

62. T. Yamashita, P. Hayes, Analysis of XPS spectra of Fe^{2+} and Fe^{3+} ions in oxide materials, Appl. Surf. Sci. 254 (2008) 2441-2449.

63. N. Xu, M. Sun, Y.W. Cao, J.N. Yao, E.G. Wang, Influence of pH on structure and photochromic behavior of nanocrystalline WO_3 Films, Appl. Surf. Sci. 157 (2000) 81-84.

64. M. Aslam, I.M.I. Ismail, N. Salah, S. Chandrasekaran, M.T. Qamar, A. Hameed, Evaluation of sunlight induced structural changes and their effect on the

photocatalytic activity of V_2O_5 for the degradation of phenols, J. Hazard. Mater. 286 (2015) 127-135.

65. T.K. Townsend, E.M. Sabio, N.D. Browningb, F.E. Osterloh, Photocatalytic water oxidation with suspended alpha-Fe_2O_3 particles-effects of nanoscaling, Energy Environ. Sci. 4 (2011) 4270-4275.

66. N. Salah, A. Hameed, M. Aslam, M.S. Abdel-wahab, S.S. Babkair, F.S. Bahabri, Flow controlled fabrication of N doped ZnO thin films and estimation of their performance for sunlight photocatalytic decontamination of water, Chem. Eng. J. 291 (2016) 115-127.

67. Y.T. Liu, Q.B. Yuan, D.H. Duan, Z.L. Zhang, X.G. Hao, G.Q. Wei, S.B. Liu, Electrochemical activity and stability of core-shell Fe_2O_3/Pt nanoparticles for methanol oxidation, J. Power Sources 243 (2013) 622-629.

68. M.T. Qamar, M. Aslam, Z.A. Rehan, M.T. Soomro, Ikram Ahmad, M. Ishaq, I.M.I. Ismail, P. Fornasiero, A. Hameed, MoO_3 altered ZnO: A suitable choice for the photocatalytic removal of chloro-acetic acids in natural sunlight exposure, Chem. Eng. J. 330 (2017) 322-336.

69. M. Aslam, M.T. Qamar, M.T. Soomro, I.M.I. Ismail, N. Salah, T. Almeelbi, M.A. Gondal, A. Hameed, The effect of sunlight induced surface defects on the photocatalytic activity of nanosized CeO_2 for the degradation of phenol and its derivatives, Appl. Catal. B: Environ. 180 (2016) 391-402.

Figure Captions

Fig. 1. The comparison of the (a) solid-state absorption spectra in 200-900 nm range (b) graphical evaluation of bandgap (c) PL spectra (d) Raman spectra of α- and γ-Fe_2O_3.

Fig. 2. The comparison of the XRD patterns of α- and γ-Fe_2O_3 in the range of 2θ = 20º - 80º.

Fig. 3. The comparison of FESEM images of α- Fe_2O_3 and γ-Fe_2O_3 at (a, b) 60kx, (c, d) 120kx and (e, f) 250kx, respectively.

Fig. 4. (a, b) The HRTEM images (c, d) the discrete fringe patterns with 0.252 nm & 0.283 nm in the single crystal and (e, f) the SAED patterns corresponding to the identified discrete spacing of α- Fe_2O_3.

Fig. 5. (a) The HRTEM image (b) the SAED patterns corresponding to the identified discrete spacing and (c, d) the identified discrete spacing of 0.283 nm in two different crystals of γ-Fe_2O_3.

Fig. 6. The comparison of (a) the wide-angle survey scan (b) Fe 2p peaks and (c) O 1s peaks of α- and γ- polymorphs of Fe_2O_3 whereas the high resolution, deconvoluted fitted Fe 2p peaks of α- and γ- Fe_2O_3 are compared in (d) and (e) respectively.

Fig. 7. The comparison of the percentage degradation (a, c) and plots of $\ln(C_o/C)$ versus sunlight exposure time (b, d) of 2-NP and 2-CP respectively, over α- and γ-Fe_2O_3.

Fig. 8. The comparison of decrease in TOC removal (a, c) and plots of $\ln(C_o/C)$ versus the sunlight exposure time (b, d) 2-NP and 2-CP over α- and γ-Fe_2O_3 in sunlight exposure.

Fig. 9. The comparison of HPLC degradation profiles (a) 2-NP, α-Fe_2O_3 (b) 2-NP, γ-Fe_2O_3 (c) 2-CP, α-Fe_2O_3 (d) 2-CP, γ-Fe_2O_3 in complete spectrum sunlight exposure.

Fig. 10. The comparison of the CV profiles (a) unexposed α-Fe_2O_3 (b) unexposed γ-Fe_2O_3 (c) exposed α-Fe_2O_3 (d) exposed γ-Fe_2O_3 in the dark and under illumination.

Fig. 11. The comparison of the EIS Nyquist plots of exposed and unexposed (a, c) α-Fe_2O_3 (b, d) γ-Fe_2O_3 in the high and low-frequency linear region under illumination.

Fig. 12. The comparison of the photocatalytic activity of exposed and unexposed α-Fe_2O_3 and γ-Fe_2O_3 for the degradation of 2-NP in the exposure of the visible region of sunlight.

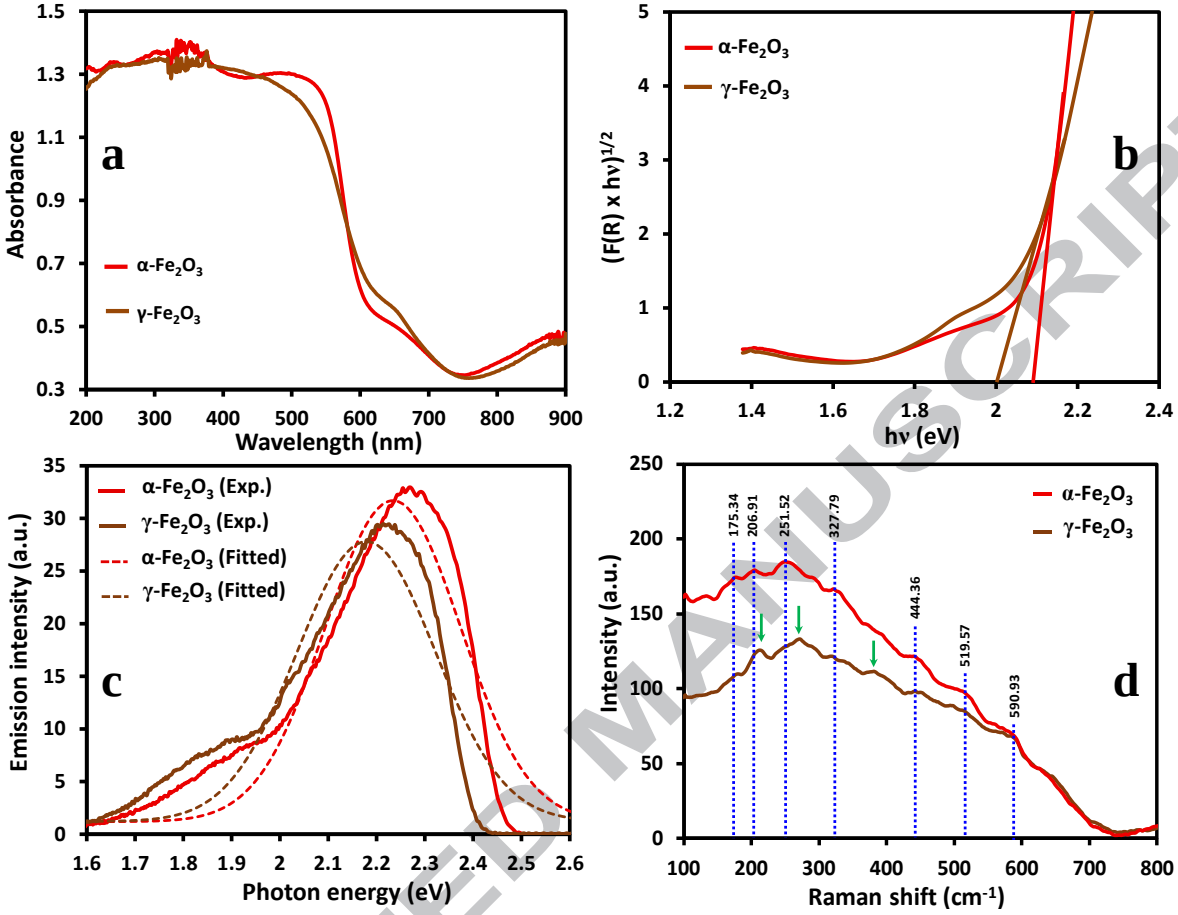

Fig. 1. The comparison of the (a) solid-state absorption spectra in 200-900 nm range (b) graphical evaluation of bandgap (c) PL spectra (d) Raman spectra of α- and γ-Fe_2O_3.

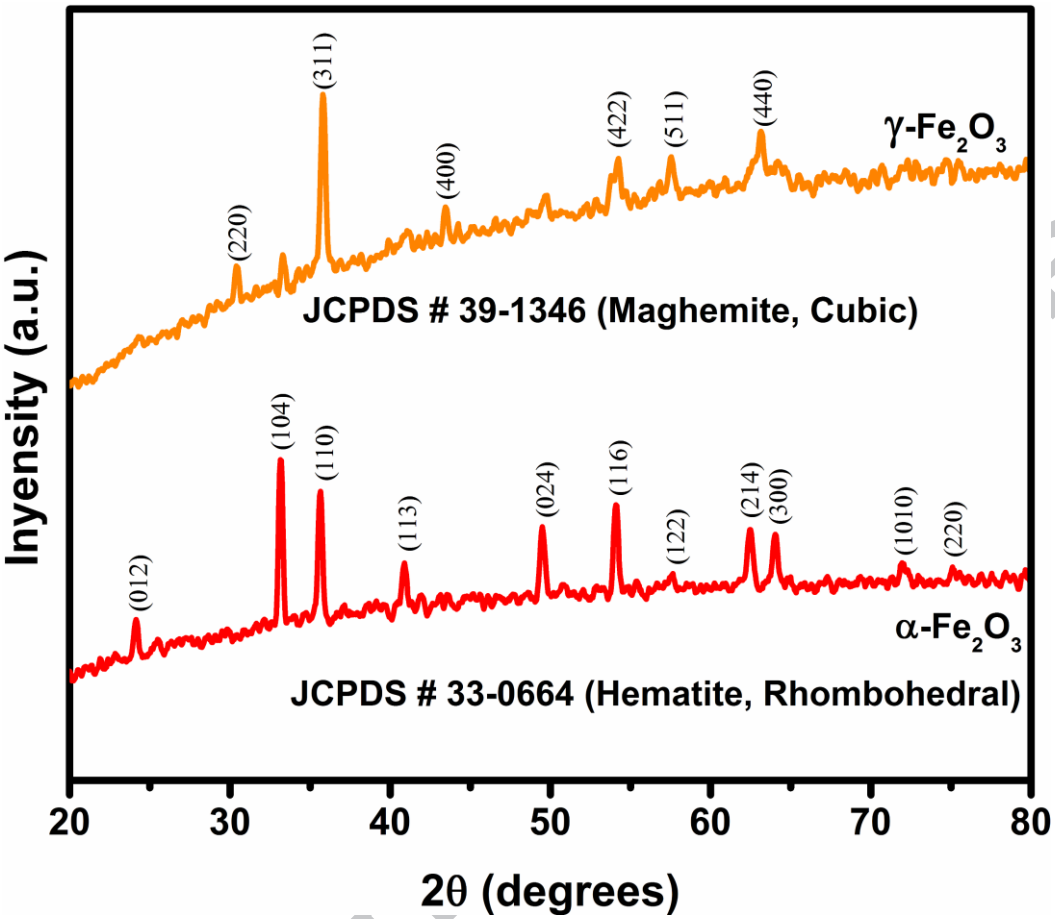

Fig. 2. The comparison of the XRD patterns of α- and γ-Fe_2O_3 in the range of 2θ = 20º - 80º.

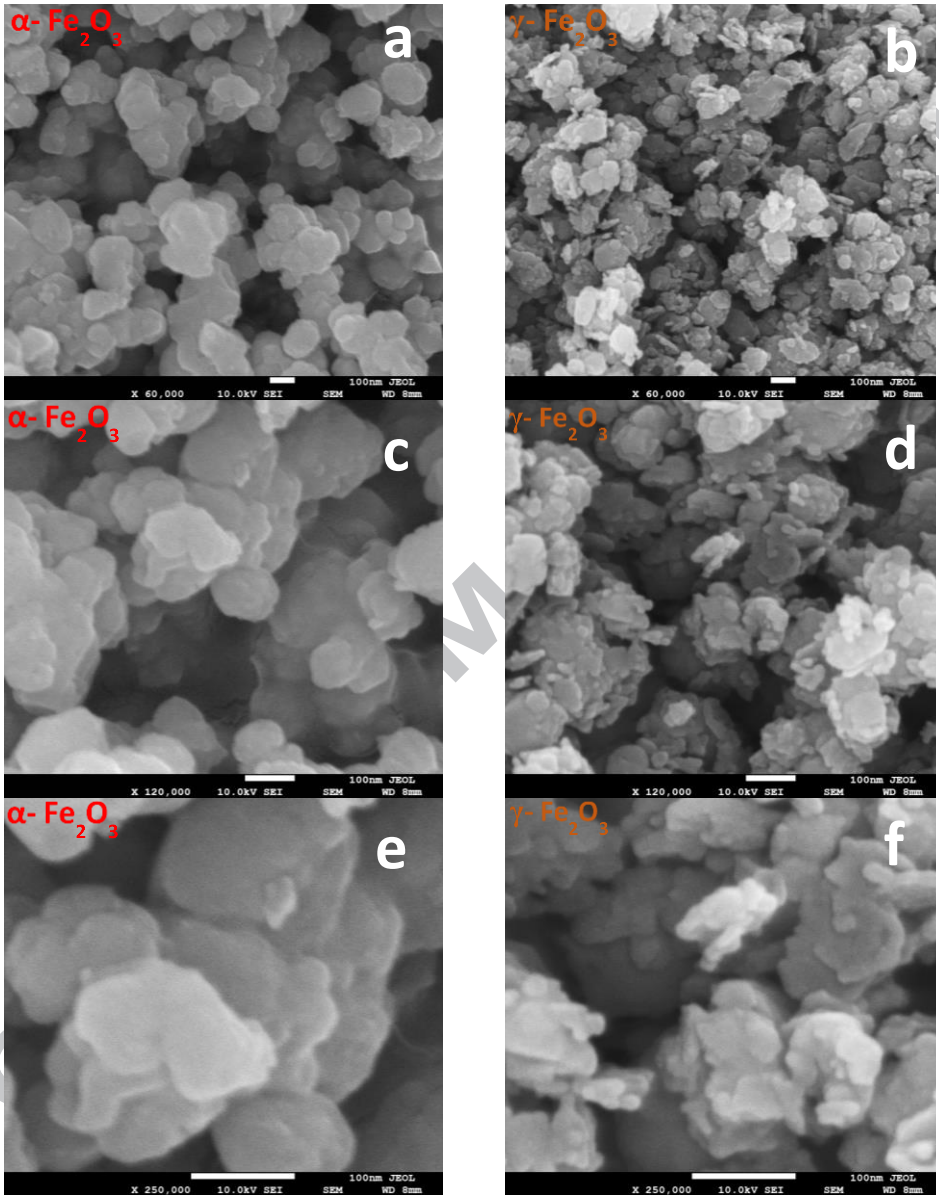

Fig. 3. The comparison of FESEM images of α- Fe_2O_3 and γ-Fe_2O_3 at (a, b) 60kx, (c, d) 120kx and (e, f) 250kx, respectively.

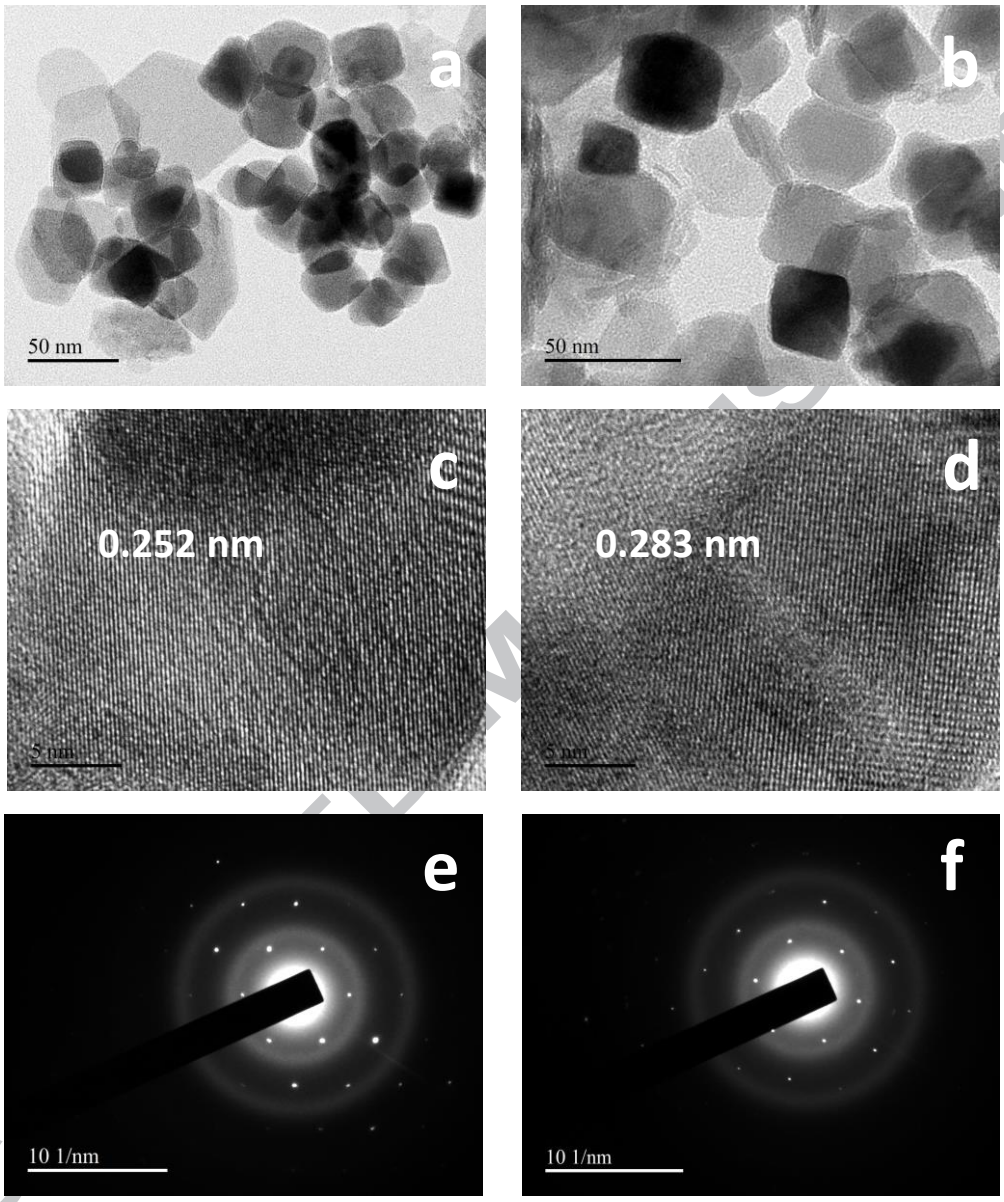

Fig. 4. (a, b) The HRTEM images (c, d) the discrete fringe patterns with 0.252 nm & 0.283 nm in the single crystal and (e, f) the SAED patterns corresponding to the identified discrete spacing of α- Fe_2O_3.

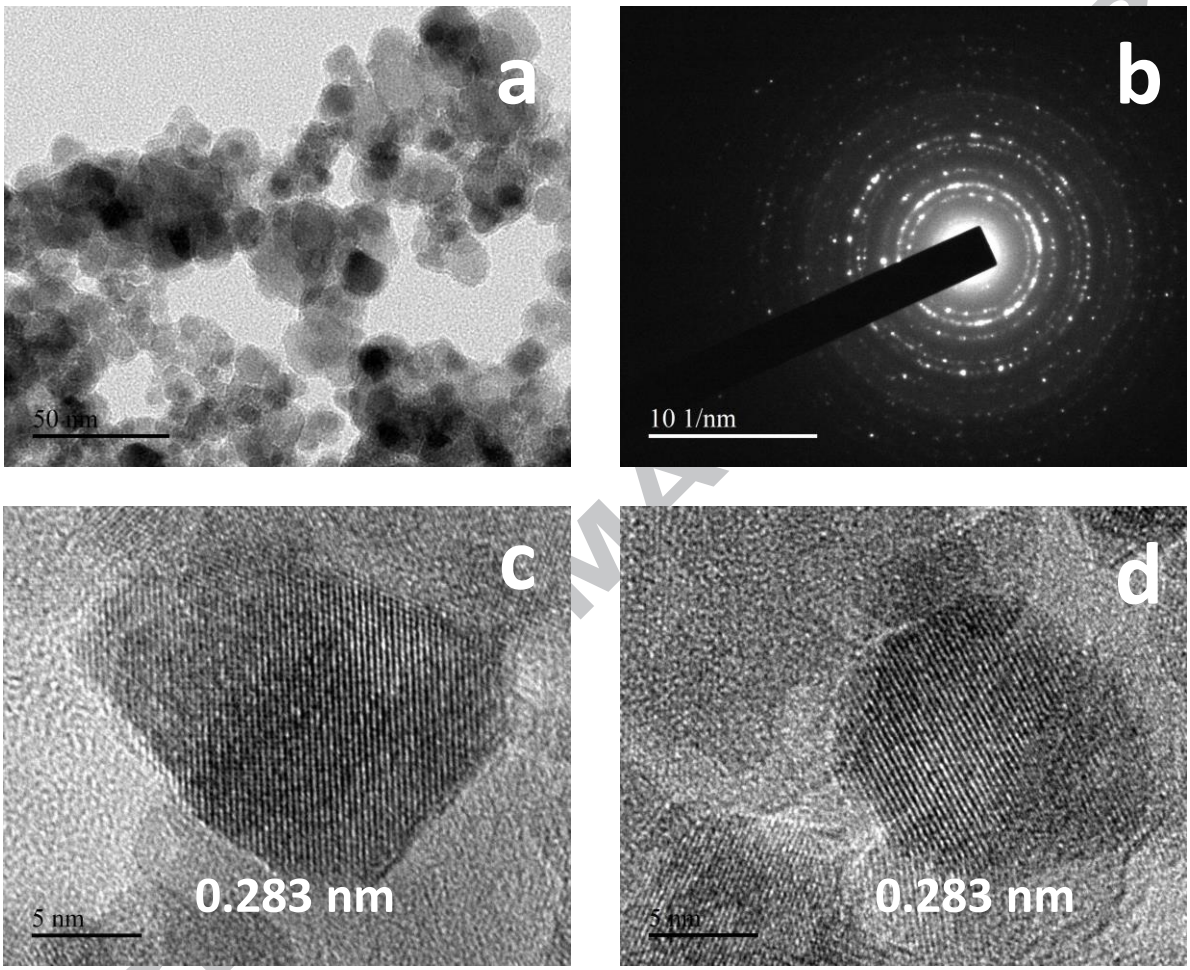

Fig. 5. (a) The HRTEM image (b) the SAED patterns corresponding to the identified discrete spacing and (c, d) the identified discrete spacing of 0.283 nm in two different crystals of γ-Fe_2O_3.

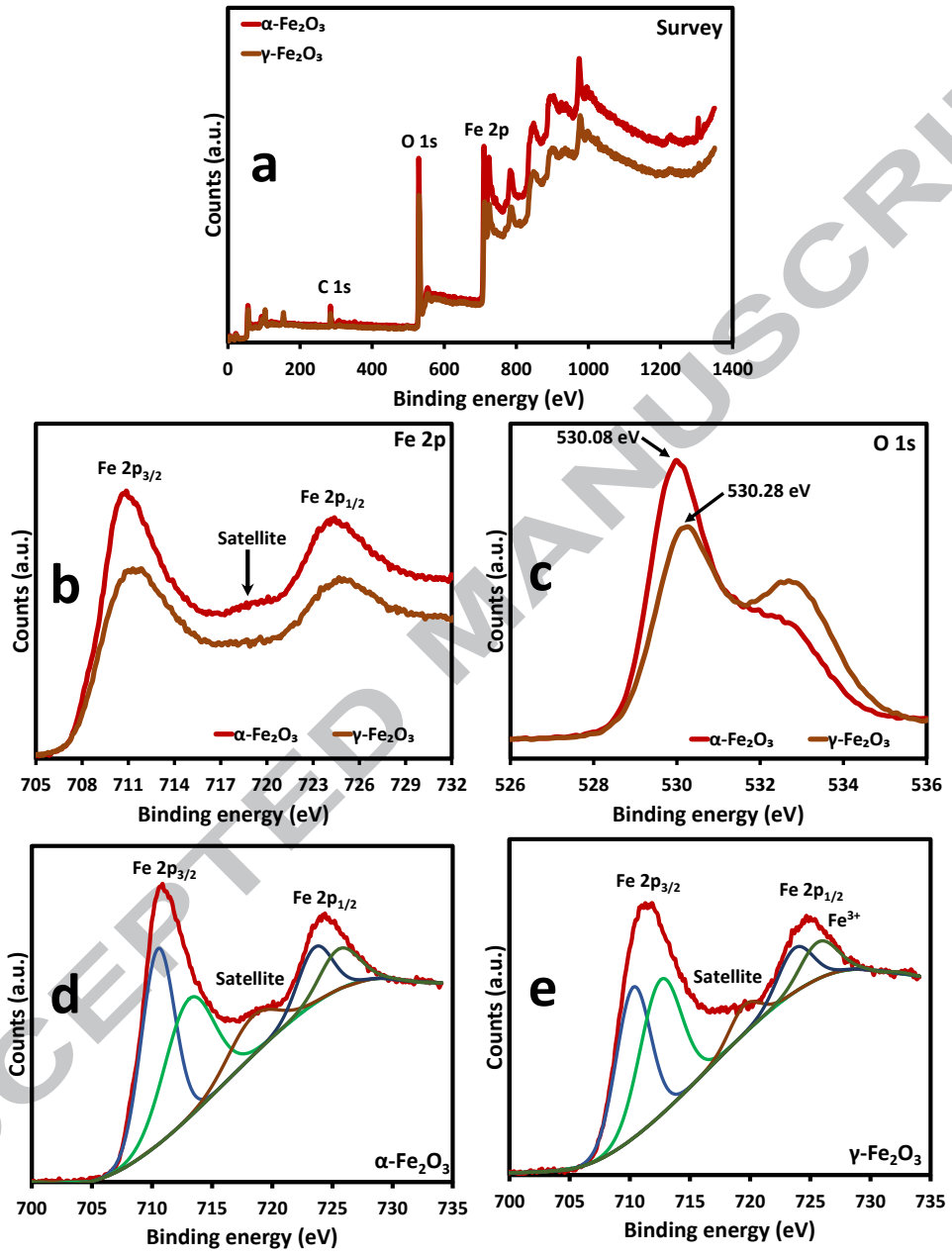

Fig. 6. The comparison of (a) the wide-angle survey scan (b) Fe 2p peaks and (c) O 1s peaks of α- and γ- polymorphs of Fe_2O_3 whereas the high resolution, deconvoluted fitted Fe 2p peaks of α- and γ- Fe_2O_3 are compared in (d) and (e) respectively.

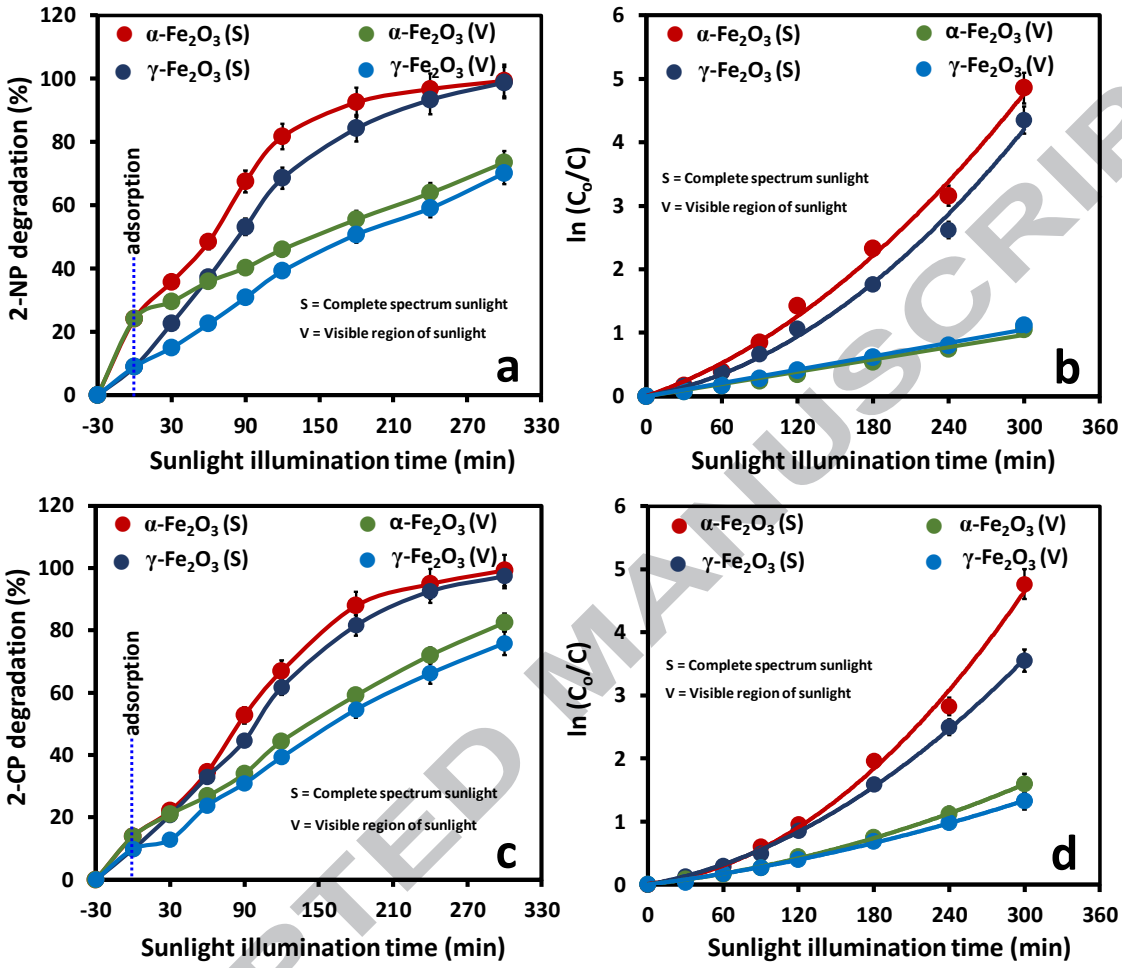

Fig. 7. The comparison of the percentage degradation (a, c) and plots of $\ln(C_o/C)$ versus sunlight exposure time (b, d) of 2-NP and 2-CP respectively, over α- and γ-Fe_2O_3.

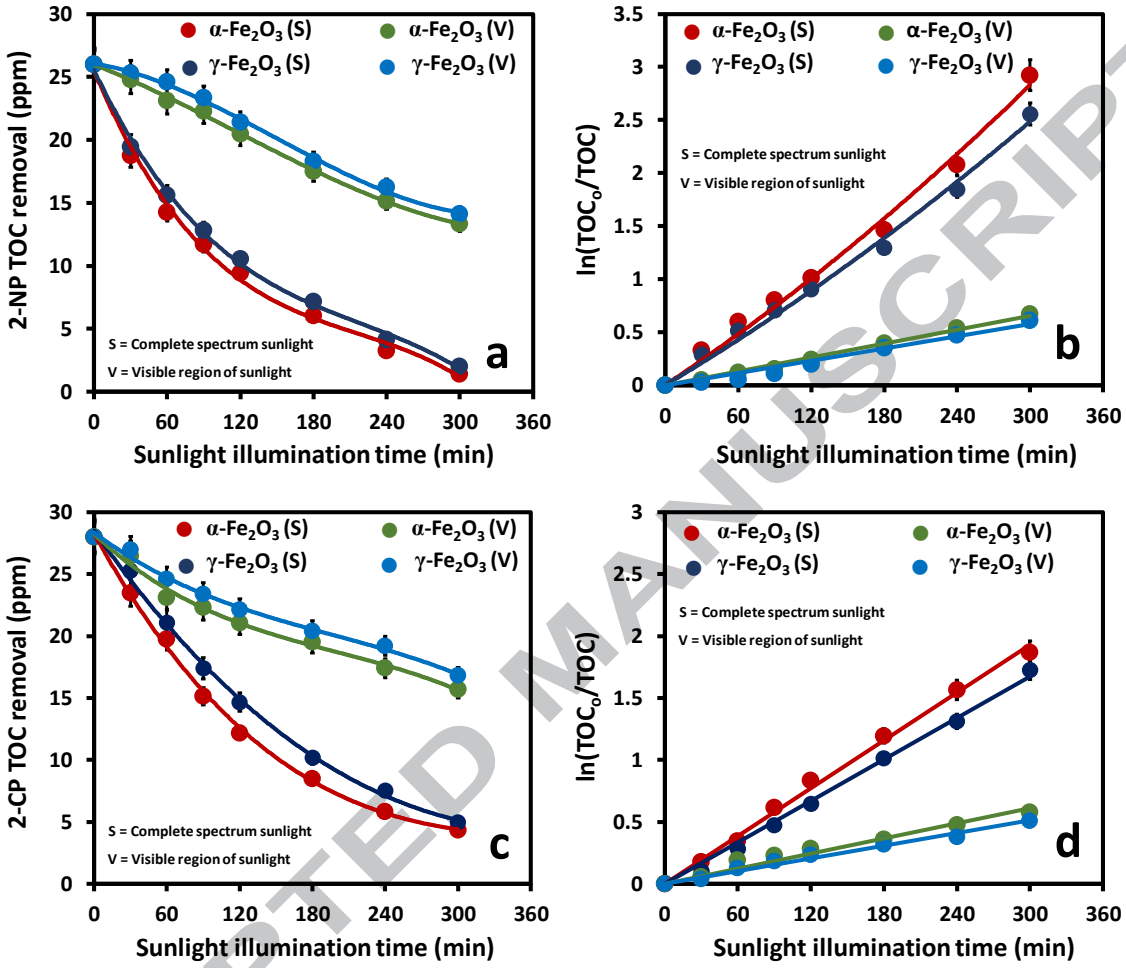

Fig. 8. The comparison of decrease in TOC removal (a, c) and plots of $\ln(C_o/C)$ versus the sunlight exposure time (b, d) 2-NP and 2-CP over α- and γ-Fe_2O_3 in sunlight exposure.

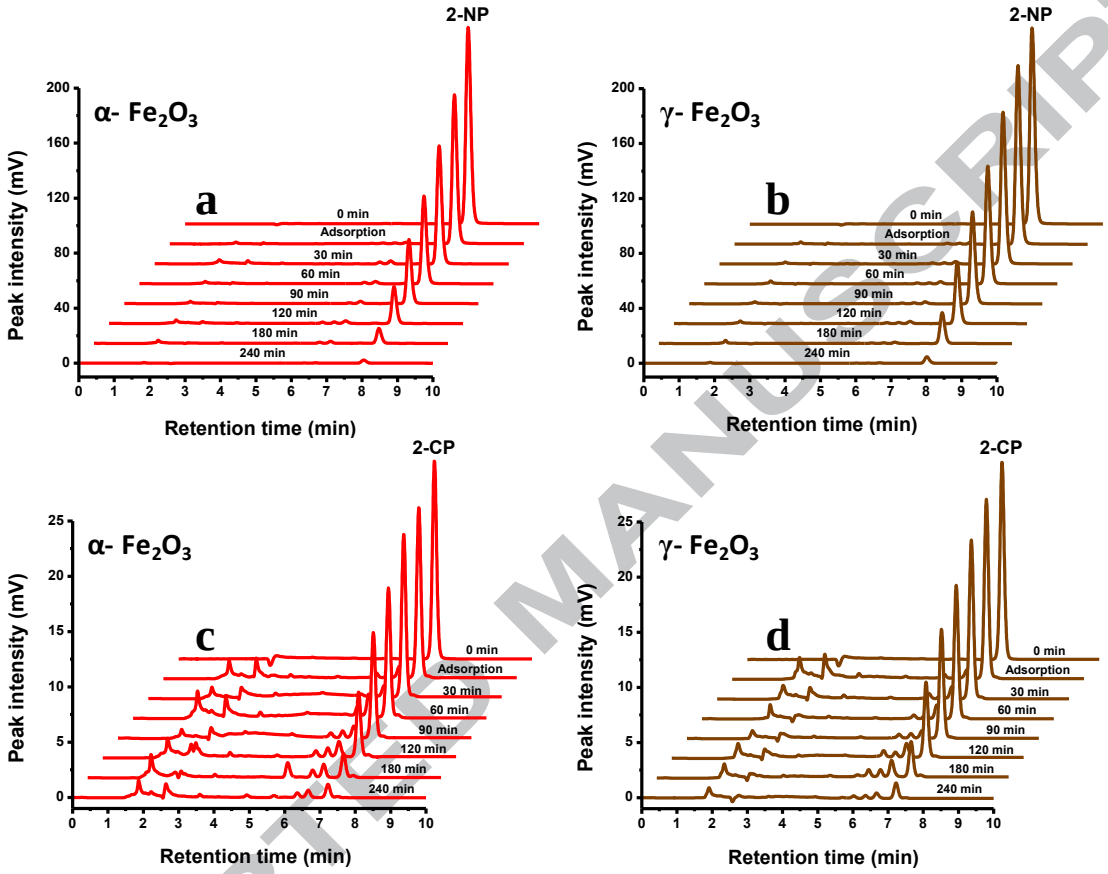

Fig. 9. The comparison of HPLC degradation profiles (a) 2-NP, α-Fe_2O_3 (b) 2-NP, γ-Fe_2O_3 (c) 2-CP, α-Fe_2O_3 (d) 2-CP, γ-Fe_2O_3 in complete spectrum sunlight exposure.

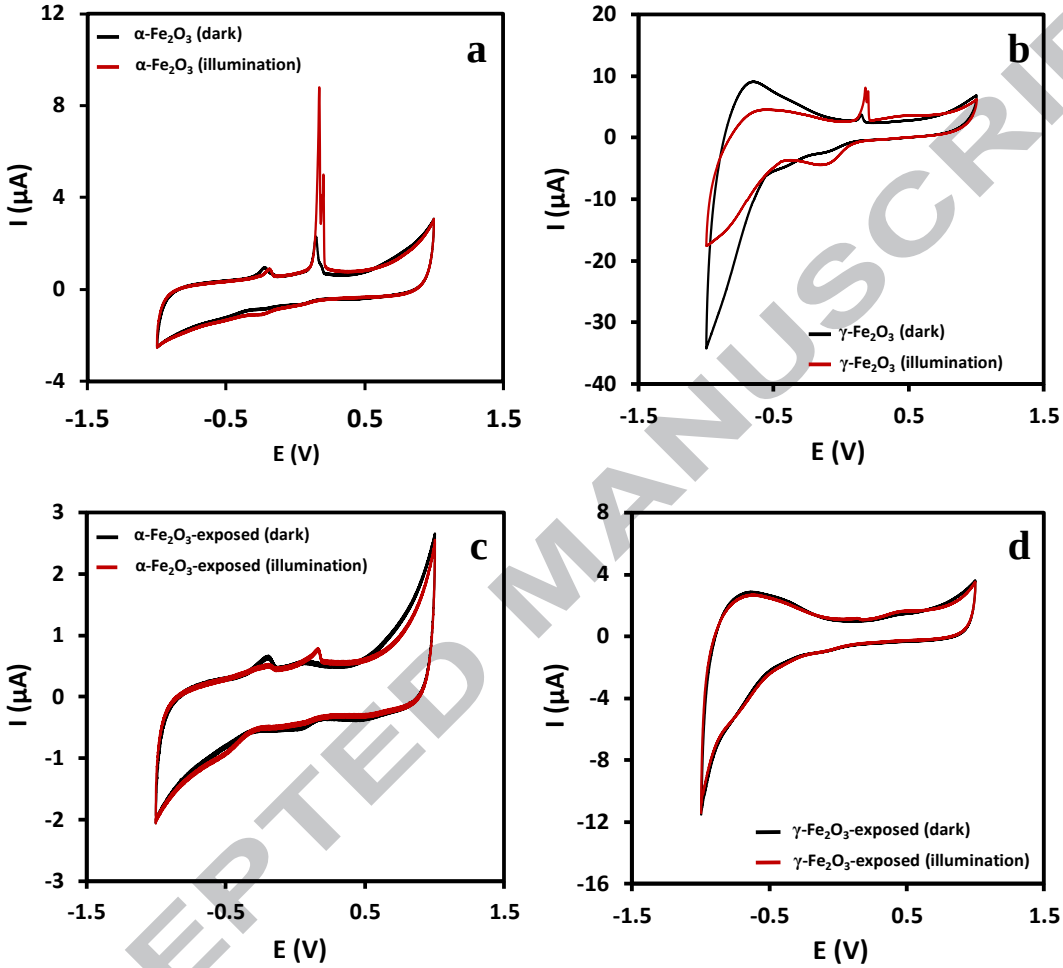

Fig. 10. The comparison of the CV profiles (a) unexposed α-Fe_2O_3 (b) unexposed γ-Fe_2O_3 (c) exposed α-Fe_2O_3 (d) exposed γ-Fe_2O_3 in the dark and under illumination.

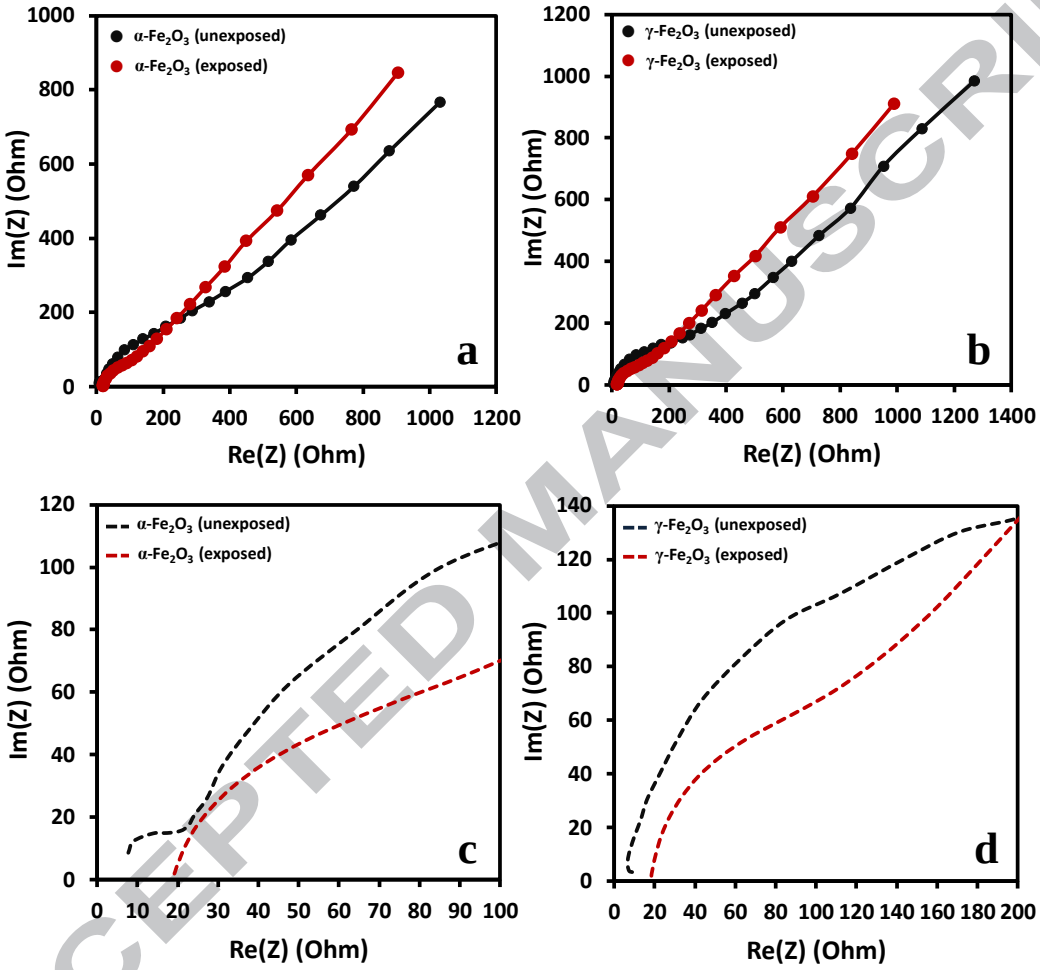

Fig. 11. The comparison of the EIS Nyquist plots of exposed and unexposed (a, c) α-Fe_2O_3 (b, d) γ-Fe_2O_3 in the high and low-frequency linear region under illumination.

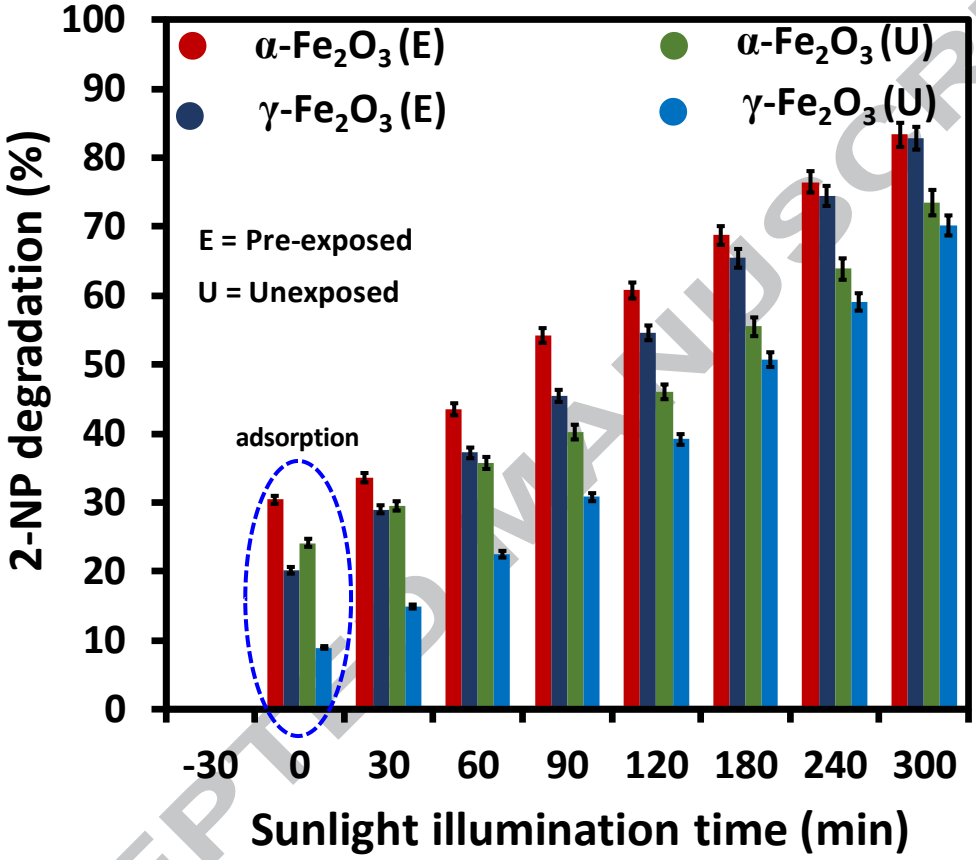

Fig. 12. The comparison of the photocatalytic activity of exposed and unexposed α-Fe_2O_3 and γ-Fe_2O_3 for the degradation of 2-NP in the exposure of the visible region of sunlight.

Graphical Abstract

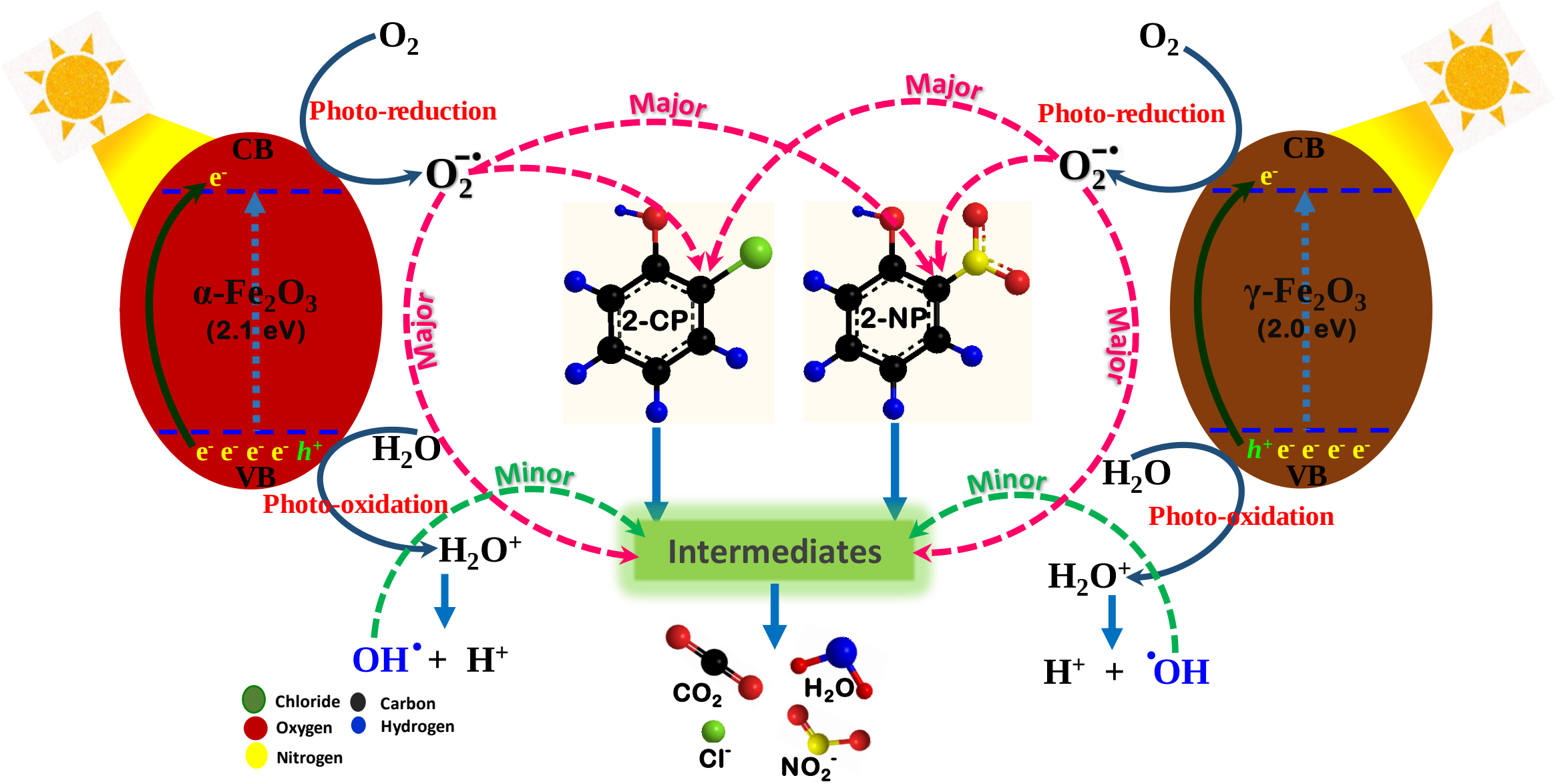

Highlights

- Facile surfactant aided hydrogel route for the synthesis of Fe_2O_3 polymorphs.
- The electrochemical measurements revealed better stability of γ-Fe_2O_3
- The photon-induced surface defects enhanced the photocatalytic activity.
- Priority interaction of ROS with the substrates rather than intermediates.
- The chloro and nitro group/s assists as initiators in the degradation process.